

**DIRECT NUMERICAL SIMULATION OF A
SEPARATED BOUNDARY LAYER**

M.Sc. THESIS

Süleyman KARACA

Department of Aeronautics and Astronautics Engineering

Aeronautics and Astronautics Engineering Graduate Programme

AUGUST 2014

**DIRECT NUMERICAL SIMULATION OF A
SEPARATED BOUNDARY LAYER**

M.Sc. THESIS

**Süleyman KARACA
(511111140)**

**Department of Aeronautics and Astronautics Engineering
Aeronautics and Astronautics Engineering Graduate Programme**

Thesis Advisor: Assist. Prof. Ayşe Gül GÜNGÖR

AUGUST 2014

**AYRILMIŞ SINIR TABAKA AKIŞININ
DOĞRUDAN SAYISAL BENZETİMİ**

YÜKSEK LİSANS TEZİ

**Süleyman KARACA
(511111140)**

Uçak ve Uzay Bilimleri Fakültesi

Uçak ve Uzay Mühendisliği Lisansüstü Programı

Tez Danışmanı: Assist. Prof. Ayşe Gül GÜNGÖR

AĞUSTOS 2014

Süleyman KARACA, a M.Sc. student of ITU Institute of Science and Technology 511111140 successfully defended the thesis entitled “**DIRECT NUMERICAL SIMULATION OF A SEPARATED BOUNDARY LAYER**”, which he prepared after fulfilling the requirements specified in the associated legislations, before the jury whose signatures are below:

Thesis Advisor : **Assist. Prof. Ayşe Gül GÜNGÖR**
Istanbul Technical University

Jury Members : **Prof. Fırat Oğuz EDİS**
Istanbul Technical University

Prof. Can Fuat DELALE
MEF University

Date of Submission : **08 Aug 2014**

Date of Defense : **18 Aug 2014**

To my wife,

FOREWORD

I would like to express my special appreciation and thanks to my adviser Dr. Ayşe Gül Güngör whose encouragement, guidance and support from the initial to the final level enabled me to develop an understanding of the subject. Without her supervision and constant help this thesis would not have been possible.

The DNS code that I used in this thesis is developed at the school of Aeronautics, Universidad Politécnica de Madrid. I would like to thank Dr. Javier Jiménez and Dr. Mark Simens for kindly sharing the source code. I would like to extend my thanks to Dr. Mark Simens for his valuable discussions and contributions.

I would like to thank my committee members, Dr. Can Fuat Delale and Dr. Fırat Oğuz Edis for serving as my committee members. I also want to thank them for letting my defense be an enjoyable moment, and for their brilliant comments and suggestions.

The research conducted in this thesis could not have been possible without the generous grants of computer time provided by Barcelona Supercomputing Center and National Center for High Performance Computing of Turkey.

An especially warm thanks go to my parents; my mother, my brother Enes and my sister Elif. It is a pleasure to acknowledge their marvelous support and encouragement.

Most of all, I would like to thank my wife Işıl for her personal support and great patience at all times. Her constant friendship, love, understanding and encouragement are enormously appreciated.

August 2014

Süleyman KARACA

TABLE OF CONTENTS

	<u>Page</u>
FOREWORD	ix
TABLE OF CONTENTS	xi
NOMENCLATURE	xiii
LIST OF TABLES	xv
LIST OF FIGURES	xvii
SUMMARY	xxi
ÖZET	xxiii
1. INTRODUCTION	1
1.1 Motivation.....	1
1.2 Literature Review	2
1.2.1 Boundary layer separation and laminar separation bubbles	2
1.2.2 Flow control for low Reynolds number flow	3
1.3 Thesis Objectives.....	6
1.4 Thesis Outline.....	7
2. NUMERICAL METHOD	9
2.1 Navier-Stokes Equations	9
2.2 Direct Numerical Simulation.....	10
2.3 Numerical Method, Geometry and Boundary Conditions.....	11
2.3.1 Implementation of roughness	14
2.3.2 Implementation of wake forcing.....	15
3. THE EFFECT OF ROUGHNESS LENGTH ON THE CONTROL OF SEPARATED BOUNDARY LAYERS	19
3.1 Introduction	19
3.2 Numerical Details.....	20
3.3 Results	21
3.3.1 Flow structures in transition region	21
3.3.2 Mean flow parameters	35
3.4 Summary.....	40
4. WAKE AND ROUGHNESS EFFECTS ON THE CONTROL OF BOUNDARY LAYERS	43
4.1 Introduction	43
4.2 Numerical Details.....	43
4.3 Results	45
4.3.1 Flow description	45
4.3.2 Mean flow statistics	47

4.3.3 Strouhal number effect 51

4.4 Summary..... 59

5. CONCLUSIONS AND FUTURE WORK..... 61

REFERENCES..... 63

CURRICULUM VITAE..... 67

NOMENCLATURE

Roman symbols

a_{APG}	: Adverse pressure gradient parameter	[1/s]
A_{ij}	: Velocity gradient	[1/s]
C_f	: Skin friction coefficient	[-]
d_w	: Diameter of cylinder generating wake	[m]
D_w	: Distance between wakes	[m]
f_i	: forcing function	[-]
h	: Roughness height	[m]
H	: Shape factor	[-]
L	: Integral length scale	[m]
L_b	: Length of the separation bubble	[m]
L_{b0}	: Length of the unforced separation bubble	[m]
L_r	: Length of the roughness	[m]
L_x, L_y, L_z	: Domain length in x, y and z coordinates	[m]
\mathcal{N}	: Number of wakes	[-]
N_x, N_y, N_z	: Number of grid points in x, y and z coordinates	[-]
p	: Pressure	[N/m ²]
P_{ij}	: First-invariant velocity gradient tensor	[1/s ²]
Q	: Second-invariant velocity gradient tensor	[1/s ⁴]
R_{ij}	: Rate-of-rotation tensor	[1/s ²]
Re	: Reynolds number based on plate length	[-]
Re_θ	: Reynolds number based on momentum thickness	[-]
S_{ij}	: Rate-of-strain tensor	[1/s ²]
St	: Strouhal number	[-]
T	: Maximum turbulent intensity	[-]
\mathcal{T}	: Wake passing period	[s]
T_{ave}	: Total average time	[s]
u'_i	: Velocity fluctuation	[m/s]
u_{rms}	: Rms of streamwise velocity component	[m/s]
u_{pb}	: Perturbation velocity	[m/s]
$\langle U \rangle$: Mean velocity	[m/s]
U_e	: External velocity	[m/s]
U_c	: Convective velocity	[m/s]
U_h	: Hiemenz velocity	[m/s]
U_{ref}	: Reference velocity at the inlet	[m/s]
U_w	: Wake velocity	[m/s]
U_{wd}	: Wake deficit velocity	[m/s]

v_{rms}	: Rms of wall-normal velocity component	$[m/s]$
w_{rms}	: Rms of spanwise velocity componen	$[m/s]$
x_r	: Reattachment location	$[m]$
x_s	: Separation location	$[m]$
x_{tr}	: Transition location	$[m]$
x_w	: Length between wake generating cylinder and leading edge of the flat plate	$[m]$
x, y, z	: Cartesian coordinate directions	$[-]$

Greek symbols

δ	: Boundary layer thickness	$[m]$
δ^*	: Displacement thickness	$[m]$
δ_{ij}	: Kronecker delta	$[-]$
ε	: Rate of kinetic energy dissipation	$[m^2/s^3]$
η	: Kolmogorov micro-scale	$[m]$
λ	: Wavelength	$[m]$
Λ_s	: Pressure gradient parameter at separation	$[-]$
μ	: Kinematic viscosity	$[m^2/s]$
ν	: Dynamic viscosity	$[kg/ms]$
$\omega_x, \omega_y, \omega_z$: Vorticity components	$[1/s]$
Ω_f	: Fluid domain	$[-]$
ρ	: Density	$[kg/m^3]$
τ_{ij}	: Reynolds stress tensor	$[kg/ms^2]$
τ_w	: Wall shear stress	$[kgm/s^2]$
θ	: Momentum thickness	$[m]$
θ_0	: Momentum thickness at the inlet	$[m]$
θ_e	: Momentum thickness at the exit	$[m]$
θ_s	: Momentum thickness at the separation	$[m]$
ξ	: Dimensionless length scale	$[-]$

Abbreviations

APG	: Adverse Pressure Gradient
BC	: Boundary condition
CFL	: Courant-Friedrichs-Lewy condition
DNS	: Direct Numerical Simulation
IBM	: Immersed Boundary Method
KH	: Kelvin-Helmholtz
LSB	: Laminar Separation Bubble
LPT	: Low Pressure Turbine
MPI	: Message Passing Interface
NS	: Navier-Stokes
rms	: Root mean square
TS	: Tollmien-Schlichting

LIST OF TABLES

	<u>Page</u>
Table 3.1 : Parameters of the roughness simulations and characteristics of the separated region. The momentum thickness, θ_0 , is measured at the inflow. x_s and x_r represent the streamwise location of the separation and reattachment point, respectively.	21
Table 4.1 : Parameters of the adverse-pressure-gradient boundary layer simulations, L_b/L_{b0} is the ratio of the length of the separated region to length of the unforced separation region.	44
Table 4.2 : Characteristics of the separated region. The parameters, x_s , x_{tr} and x_r are calculated at the separation, transition and reattachment locations respect to inflow momentum thickness, θ_0	44

LIST OF FIGURES

	<u>Page</u>
Figure 1.1 : The mean flow structure of a two-dimensional short laminar separation bubble (Horton 1968).	3
Figure 2.1 : Schematic drawing of the experimental model of the wake forcing case [1].	12
Figure 2.2 : The numerical setup and the instantaneous visualization of the spanwise vorticity in an adverse pressure gradient turbulent boundary layer. The vortices are colored with the distance to the wall; blue (dark) near the wall, and red near the top. Flow is from bottom-left to top-right.	13
Figure 2.3 : Schematic drawings of the cross-section (top) and three-dimensional (bottom) views of the discrete surface roughness.	15
Figure 2.4 : Wake velocity deficit profile respect to the free-stream velocity.	16
Figure 2.5 : Schematic drawings of numerical model of the wake forcing case... ..	17
Figure 3.1 : Instantaneous snapshots of spanwise vorticity contours. Top: $\mathcal{R}3d$; bottom: $\mathcal{R}3dL$. Flow is from bottom to top right, and the box is $650\theta_0 \times 120\theta_0 \times 260\theta_0$. The isosurface is colored by the distance to the wall, from $y/\theta_0 = 0$ for the deepest blue, to $y/\theta_0 = 50$ for the brightest red. Note roughness height $h = 0.7\theta_0$	23
Figure 3.2 : Instantaneous snapshots of second-invariant of the velocity gradient tensor. Top: $\mathcal{R}3d$; bottom: $\mathcal{R}3dL$. Flow is from bottom to top right, and the box is $650\theta_0 \times 120\theta_0 \times 260\theta_0$. The isosurface is colored by the distance to the wall, from $y/\theta_0 = 0$ for the deepest blue, to $y/\theta_0 = 50$ for the brightest red. Note roughness height $h = 0.7\theta_0$	24
Figure 3.3 : Streamwise vorticity contours, (a) $\mathcal{R}3d$ and (b) $\mathcal{R}3dL$ on xz plane and $y/\theta_0 = 5$. $0 < \omega_x/\omega_x _{max} < 1$. The magenta lines represents the locations of $x/\theta_0 = 60, 84, 132$ and 226	26
Figure 3.4 : Streamwise vorticity contours(shaded contours) of the surface trip of the cases $\mathcal{R}3d$ and $\mathcal{R}3dL$ on yz plane at different x locations. $0 < \omega_x/\omega_x _{max} < 1$. The arrows are the cross flow (v, w) velocity vectors, and the magenta line is the zero contour of the streamwise velocity. Left column: $\mathcal{R}3d$, Right column: $\mathcal{R}3dL$. From top to bottom, $x/\theta_0 = 60, 84, 132$ and 226	27

Figure 3.5 :	Streamwise velocity contours in xz plane of the cases $\mathcal{R}3d$. Dark red contours after the roughness element are positive streaks and blue contours are negative streaks. Top: inside the roughness ($y/\theta_0 = 0.3$), Bottom: outside the roughness ($y/\theta_0 = 20$)	29
Figure 3.6 :	Streamwise velocity contours in xz plane of the cases $\mathcal{R}3dL$. Dark red contours after the roughness element are positive streaks and blue contours are negative streaks. Top: inside the roughness ($y/\theta_0 = 0.3$), Bottom: outside the roughness ($y/\theta_0 = 20$)	30
Figure 3.7 :	Streamwise evolution of the u'/U_e in a wall-parallel at $y/\theta_0 = 0.5$. (a) $\mathcal{R}3d$; (b) $\mathcal{R}3dL$. Black and magenta lines denote the streamwise extent of the roughness and separation bubble, respectively.....	31
Figure 3.8 :	(a) u'/U_e and (b) $d\langle U \rangle dy$. - - - : $x/\theta_0 = 50$; - - - - : $x/\theta_0 = 165$; — : $x/\theta_0 = 200$. Green: $\mathcal{R}3d$, Red: $\mathcal{R}3dL$	32
Figure 3.9 :	Evolution of the transitional structures of the $\mathcal{R}3d$ case at three different time instances t_1 , t_2 and t_3 . Isosurface of the second-invariant of the velocity gradient tensor colored by the distance to the wall, from $y/\theta_0 = 0$ for the deepest blue, to $y/\theta_0 = 50$ for the brightest red. Flow is from bottom left to top right.....	33
Figure 3.10 :	Evolution of the transitional structures of the $\mathcal{R}3dL$ case at three different time instances t_1 , t_2 and t_3 . Isosurface of the second-invariant of the velocity gradient tensor colored by the distance to the wall, from $y/\theta_0 = 0$ for the deepest blue, to $y/\theta_0 = 50$ for the brightest red. Flow is from bottom left to top right.....	34
Figure 3.11 :	Mean spanwise vorticity contours, $0 < \omega_z/\omega_{z,max} < 1$ (a) $\mathcal{R}W0$, (b) $\mathcal{R}3d$ and (c) $\mathcal{R}3dL$. Black line: boundary layer thickness, white dashed line: inflection point, magenta line: zero contours of streamwise velocity.	36
Figure 3.12 :	Root mean square contours of the velocity fluctuations in xy plane of the cases $\mathcal{R}W0$, $\mathcal{R}3d$ and $\mathcal{R}3dL$. From left to right: u_{rms} , v_{rms} , and w_{rms} ; from top to bottom: $\mathcal{R}W0$, $\mathcal{R}3d$, and $\mathcal{R}3dL$. The rms values are normalized with the maximum value of each other, $0 < u_{i,rms}/u_{i,rms,max} < 1$. The magenta lines represent the length of the roughness element.	37
Figure 3.13 :	Streamwise evolution of the (a) skin friction coefficient; (b) shape factor; (c) separation bubble; (d) maximum turbulent intensity. Black: Smooth, Green: $\mathcal{R}3d$, Red: $\mathcal{R}3dL$. — : separated flow, $C_f < 0$, and - - - - : attached flow, $C_f > 0$. Vertical dashed lines denote the streamwise extent of the roughness field.....	38
Figure 3.14 :	Streamwise evolution of the y_{max}/y_{inflec} . Green: $\mathcal{R}3d$, Red: $\mathcal{R}3dL$. Vertical dashed lines denote the streamwise extent of the roughness field.	40

Figure 4.4 :	The development of the negative wall shear stress as a function of space and time. Top: $\mathcal{R}3dWSt0.78$; bottom: $\mathcal{R}3dWSt1.55$. The blue line traces the wake center and the magenta one waves generated by the wake. The propagation speed of these waves is $0.45U_e$. The vertical lines mark roughness, separation, transition, and reattachment points of the time averaged bubble.	52
Figure 4.5 :	The phase-averaged skin friction coefficient over one forcing period for case $R3dWSt0.78$. The vertical thick solid line marks the location of the wake center.	55
Figure 4.6 :	The phase-averaged skin friction coefficient over one forcing period for case $R3dWSt1.55$. The vertical thick solid line marks the location of the wake center.	56
Figure 4.9 :	The effects of wake forcing (green diamond), surface roughness (blue circle), and combined effect of roughness and wake (red triangle) on the size of the separation bubble, L_b	59

DIRECT NUMERICAL SIMULATION OF A SEPARATED BOUNDARY LAYER

SUMMARY

The main factor that determines the efficiency of a low-pressure-turbine is the size of the laminar separation bubble that forms on the suction side of the turbine blade. A laminar separation bubble occurs when a laminar boundary layer separates in the presence of an adverse streamwise pressure gradient, undergoes laminar-to-turbulent transition through the amplification of disturbances within the flow, and then reattaches due to the enhanced wall-normal momentum exchange arising from turbulence. In this study, the suction side of a low-pressure gas-turbine blade is modeled as a flat plate with a streamwise pressure distribution. The effects of discrete surface roughness and periodic large-scale wake forcing on separation bubble transition and control are investigated numerically by direct numerical simulation. The three-dimensional discrete roughness with varying roughness height in the spanwise direction is modeled using immersed boundary method. The wake effect is numerically modeled as the mean wake deficit profile created by a linear row of cylinders moving in a direction perpendicular to the flat plate. Results indicate that the location of transition—and hence the shape and extent of the separation bubble—largely depend on which of the above-noted passive control mechanisms dominates the transition process. The laminar separation bubble is controlled by positioning the roughness element upstream of the separation bubble and introducing a low-frequency large-scale wake forcing.

AYRILMIŞ SINIR TABAKA AKIŞININ DOĞRUDAN SAYISAL BENZETİMİ

ÖZET

Düşük basınçlı türbinlerin verimliliğini etkileyen en önemli faktör türbin palasının emme bölgesinde oluşan laminar ayrılma baloncuğunun boyutudur. Laminar ayrılma baloncuğu, ters basınç gradyanı sebebiyle laminar sınır tabakada akışın duvardan ayrılmasıyla, akışla birlikte gelen bozuntuların büyüklüğünün artması ile akışın laminardan türbülansa geçmesi ve duvar doğrultusunda türbülansdan kaynaklanan momentum alış-verişinin artması sebebiyle akışın duvarla yeniden birleşmesiyle oluşur. Bu çalışmada, düşük basınçlı gaz türbinin emme bölgesi düz bir plaka üzerinde akış doğrultusunda basınç dağılımı tanımlanarak modellenmiştir. Ayrık yüzey pürüzlülüğü ve periyodik iz bölgesinin ayrılma baloncuğunun laminardan türbülansa geçişi ve bu geçiş mekanizmasının kontrolü üzerindeki etkileri doğrudan sayısal benzetim yöntemiyle incelenmiştir. Yüksekliği kanat açıklığı doğrultusunda periyodik olarak değişen üç boyutlu yüzey pürüzlülük elemanı gömülü sınır yöntemi kullanılarak modellenmiştir. İz etkisi, plakaya dik doğrultuda hareket eden lineer şekilde sıralanmış silindirlerin arkasında oluşan ortalama iz profili ile sayısal olarak modellenmiştir. Sonuçlar, laminardan türbülansa geçiş bölgesinin konumu ve dolayısıyla laminar ayrılma baloncuğunun şekli ve genişliğinin yukarıda bahsedilen, laminardan türbülansa geçiş sürecini yöneten pasif kontrol elemanlarına bağlı olduğunu göstermiştir. Laminar ayrılma baloncuğu, pürüzlülük elemanını ayrılma bölgesinden önceye konumlandırarak ve düşük frekansta iz bölgesi etkisi tanımlanarak kontrol altına alınabilir.

1. INTRODUCTION

1.1 Motivation

Energy saving and fuel emission are of great interest, especially for civil and military aviation because of the increase in fuel prices and environmental reasons. The low pressure turbine (LPT) section of an aviation gas turbine engine is a very significant part of the engine in most respects. The weight of the LPT is approximately 1/3 of the whole engine. Furthermore, in terms of fuel efficiency, a small amount of increase in LPT aerodynamics efficiency results in drop in fuel consumption and emission.

The main factor that determines the efficiency of a LPT is the extent and size of the separation bubble that forms on the low pressure side of the turbine blade. In a modern aircraft engine, the LPT blades experience low Reynolds numbers, typically in the range of 0.5×10^5 to 5×10^5 [2]. In general, at these Reynolds numbers, the flow on the low pressure side of the turbine blade is laminar at the leading edge, decelerated due to an adverse pressure gradient, which causes the flow to separate and transition to turbulence close to the trailing edge [2]. Moreover, during the service operation, LPT airfoils are exposed to different aerodynamic loadings. For instance, the aerodynamic loading of the LPT airfoils increases during take-off which causes a growth of the adverse pressure gradient on the suction side, the boundary layer thickness grows and a laminar separation bubble forms and increases in size as well. The efficiency of the LPT blade will, therefore, decrease.

Experiments show that the dominant effect on the boundary layer loss is generated by the suction side of the LPT blade, and the size of the laminar separation bubble (LSB) determines the magnitude of the profile drag. Therefore, if we reduce the size of the LSB, we will decrease the profile drag. Since, for low Reynolds number flows, the main part of the drag comes from profile (pressure) drag rather than skin friction drag, then the net drag force will reduce as well.

Therefore, in order to increase the blade efficiency, the laminar separation bubble must be controlled by active or passive flow control mechanisms [3].

1.2 Literature Review

1.2.1 Boundary layer separation and laminar separation bubbles

Leaving off of the flow from the solid surface due to the dissipation, mostly due to adverse pressure gradient (APG) is called separation. An APG causes the streamwise velocity to decrease along the streamwise direction and, if it is strong enough, the velocity goes to zero and separation occurs. The separation point can be defined as a location between the forward and backward flow, where the shear stress is zero

$$\tau_w = \mu \left. \frac{du}{dy} \right|_{y=0} = 0. \quad (1.1)$$

Here, u is the streamwise velocity, y is the wall-normal direction, and μ is the viscosity. The region where the flow reattaches to the surface is called reattachment point. This closed separated volume is called laminar separation bubble (see Figure 1.1). Laminar separation bubble is a vortical structure, which is generated inside the separated zone, moving the separated flow in opposite direction of the main flow. So, LSB represents a closed zone and, inside this separated zone, the flow stays almost steady. There is almost no energy exchange between this separated zone and the outer flow.

When the flow separates from the surface, pressure (profile) drag increases due to increasing size (height and length) of the boundary layer. If the separated flow does not reattach to the wall, complete separation occurs. This is a "stall" condition, as it is known. In this condition, there is almost no lift, very high drag and imbalances in the pitching moment. This is the reason of the instability which causes the control problem of the vehicle and, the consequences of this may catastrophic.

The size and length of the LSB are highly correlated with the strength of the APG and Reynolds number. In literature, there are two types of LSBs; "long separation bubble" and "short separation bubble". The type of the bubble is determined by the displacement thickness at the separation point [4]. The displacement thickness for incompressible flow is defined as the distance a streamline just outside the boundary

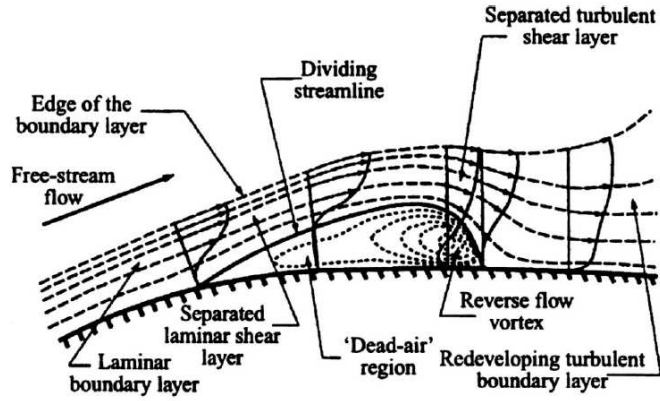


Figure 1.1: The mean flow structure of a two-dimensional short laminar separation bubble (Horton 1968).

layer is displaced away from the wall compared to the inviscid solution and given by the following equation:

$$\delta^* = \int_0^{\infty} \left(1 - \frac{u}{U_0}\right) dy. \quad (1.2)$$

where U_0 is the free-stream velocity outside the boundary layer.

The bubble is long if the parameter $1/\delta_s^* \sim O(10^2)$ and short if the parameter $1/\delta_s^* \sim O(10^4)$ [5]. Here, δ_s^* refers to the displacement thickness at the separation point. Pressure distribution of a long bubble is quite different from that of inviscid (potential) flow [4]. Thus, long bubble has negative effect on the aerodynamic efficiency of the structure. For cases studied in this thesis, the δ_s^* is between 0.0017 and 0.0021 which corresponds to an interval between 450 and 600 for $1/\delta_s^*$. According to the definition given above, our separation bubbles are neither too short nor too long.

1.2.2 Flow control for low Reynolds number flow

Flow control is any technique, mechanism or process to force to change characteristics or arrangements of the flow field. The aim of the flow control is to increase the aerodynamic efficiency of the geometry/vehicle/device, by reducing the drag or by the recovery of the pressure distribution to the inviscid form, by interfering the flow in boundary layer using various flow control techniques. Shortly, desired target in flow control can be summarized as delay of boundary layer separation, wake management and boundary layer mixing [6].

In literature, flow control mechanisms can be divided as passive control and active control. Passive flow control techniques, such as roughness and wake passing frequency, do not need any additional power opposed to the active flow control techniques. However, while passive control is steady in time, active techniques can change its position, location or shape in time depending on different flow regimes. It is important to note that a flow control mechanism which is valid for a specific flow regime may not be valid or efficacious for another flow regime. For instance, a passive control strategy successful at low Reynolds number may not be successful at higher Reynolds numbers. Therefore, the selection of the active or passive flow control mechanisms is important and it must be done by considering the flow regime. For a broader review of the flow control methods, book written by Gad-el-Hak [7] is an excellent source.

The efficiency of LPTs is influenced by the extent and size of the separation bubble that forms on the low pressure side of the turbine blade. An increase in efficiency requires the ability to control the size of this bubble, without unduly moving the laminar-turbulent transition point upstream. Since, we are dealing with low Reynolds number flows, we use passive control methods such as surface roughness element and wake forcing in this thesis.

LPT blades contain complex flow phenomena with unsteady separation due to APG, reattachment, surface roughness, and wake interactions from the previous blade. These factors control the efficiency of the LPT. In particular, wake flow impinges on the surface of the following turbine blade and periodically changes the portion of the laminar boundary layer to turbulent and affects the turbine aerodynamics, efficiency, performance and heat transfer. Obviously a lot of study has been undertaken to understand the effects of Reynolds number, streamwise pressure gradient, periodic large-scale unsteadiness, surface roughness and small perturbations on the separation bubble [8] [9] [10] [11]. Some of these studies are briefly discussed here.

Effects of unsteady wakes on very high lift airfoils are investigated experimentally in [12] [2] and many other articles. These studies show that, in the case of low Reynolds number and very high-lift (aggressive) airfoils, without the wake effect the boundary layer separates, but does not reattach. Whereas this characteristic of the boundary layer

changes when the wake effect is introduced. For the low wake passing frequency, the boundary layer separates between wakes then reattachment occurs. In the case of high wake passing frequency, the separation bubble size decreases significantly since there is not enough time between each wake passing for the separation bubble to regenerate itself. Overall, these experimental studies reported that the reattachment of the boundary layer is due to the wakes shed by the upstream rods.

Apart from time dependent fluctuations, time independent fluctuations have been studied in [13]. In general these fluctuations are generated by a tripwire, with or without a spanwise variation, but roughness also falls into this category. Although these perturbations have a lower growth rate than the time dependent fluctuations, they are still important because they are easier to implement and/or they occur naturally on used turbine blades. The work done on this subject can be broadly divided in two branches, namely a branch that concentrates on the engineering aspect of these perturbations and a branch which is more academic [14]. The difference is mostly due to differences in the Reynolds number (high in the first branch and relatively low in the second branch) and in the manner the perturbations are imposed (real roughness and trip wires in the first branch and certain blowing and suction profiles in the second).

The experimental studies, which investigate the effect of roughness height, their location and their types, indicate that the boundary layer development depends on these roughness parameters [15]. Optimum values of these variables depend on the flow conditions. Therefore, the operational range must be wide enough in the design of the passive control mechanisms. In the case of low Reynolds numbers and low free stream turbulence, the laminar separation bubble is suppressed substantially by the roughness effect [16]. Earlier experimental and numerical studies indicate that the laminar-turbulent transition mechanism is strongly affected by the presence of localized roughness. The two-dimensional roughness element accelerates the transition process by tripping the boundary layer. The effect of a three-dimensional tripwire (the tripwire has a varying height along the spanwise direction) on boundary layers subject to adverse-pressure gradient has been discussed in [8]. Results indicate that the laminar separation and turbulent transition are mainly affected by the type, the

height and the location of the roughness element, and the separation bubble can be controlled by positioning the roughness element away from the separation bubble.

These earlier studies that show the individual effect of wakes and roughness on low-pressure turbine type boundary layer flows revealed an important question. What will happen to the boundary layer development and hence the LPT blade efficiency when combining the effects of roughness and wakes?

The purpose of this research is to search for answers to this question and to provide some insight into the underlying mechanism for roughness and wake-induced transition. This will lead to several control strategies, which is particularly important for aerodynamic and turbo-machinery applications where the early transition to turbulence leads to a significant reduction in the separated region and hence, the pressure loss.

1.3 Thesis Objectives

In this work, the study of discrete roughness and wake effect on a laminar separation bubble formed on a flat plate boundary layer due to a strong APG similar to those encountered on the suction side of typical LPT blade is carried out with direct numerical simulation approach. This would complement, to a certain degree, previous works [8] [9] that have emphasized the individual effect of roughness and unsteady wake forcing in laminar separated boundary layers. In particular, the major objectives of this thesis are:

- To investigate the effect of roughness length on transition and separated region.
- To study the combined effect of roughness and wake forcing on the control of separated boundary layer.
- To provide detailed steady and unsteady boundary layer flow information to clarify the underlying physics of the separation bubble under the unsteady wake and discrete roughness effects.
- To identify the key parameters for LPT efficiency.
- To constitute a database for academic and industrial studies.

1.4 Thesis Outline

This thesis is organized as follows: The research motivation and the literature review are given in Chapter 1. Numerical method is described in Chapter 2, the DNS code is briefly reviewed, details of the numerical implementation of the roughness, and the wake forcing are presented. The effect of roughness length with varying roughness height in the spanwise direction, like a wave form on the separated boundary layer, is given in Chapter 3. First, a brief introduction and some numerical details about the roughness simulation are given. Some flow structures in the transition region are presented and the streamwise evolution of the mean flow characteristics are examined in the results section. The combined effect of wake forcing and surface roughness are presented in Chapter 4. The shape of the roughness element is kept constant while the wake passing period is changed. Effects of two different wake passing periods with surface roughness on the separated boundary layers are presented. The details of the flow are described and mean flow statistics are presented. Then, the Strouhal number effect is presented on space-time diagrams, introducing phase averaged boundary parameters and structures in transition region. Finally, conclusions and recommendations for future work are given in Chapter 5.

The results presented in this thesis have been partly published in the following conference proceedings,

- Gungor, A.G., Karaca, S., and Simens, M.P., "The influence of roughness length on the control of separation bubbles," 10th International ERCOFTAC Symposium on Engineering Turbulence Modeling and Measurements, Malaga, Spain, 2014.
- Gungor, A.G., Simens, M.P., and Karaca, S., "Direct numerical simulation of roughness and unsteady wake effect on separated boundary layers", 14th European Turbulence Conference, Lyon, France, 2013.
- Karaca, S., Simens, M.P., and Gungor, A.G., "Direct numerical simulation of combined effects of wake and discrete surface roughness on separated boundary layers," 7th Ankara International Aerospace Conference, Ankara, Turkey, 2013.

- Karaca, S. and Gungor A.G., "Gaz türbini pallerindeki akış ayrılmasına iz ve pürüzlülük etkilerinin DNS yöntemiyle incelenmesi ", 18th Ulusal Mekanik Kongresi, Manisa,Türkiye, 2013.

2. NUMERICAL METHOD

A brief introduction to the Navier-Stokes equations and a short overview and some background information on DNS, followed by the explanation of the numerical method are given in this section.

2.1 Navier-Stokes Equations

In this chapter the equations governing the evolution of an incompressible (constant density) Newtonian fluid are presented. The velocity is assumed to be sufficiently low so that the compressibility effects can be neglected. Therefore, the continuity equation and the momentum equation completely describe the flow field.

For a constant density flow the conservation of mass is given by

$$\frac{\partial u_i}{\partial x_i} = 0, \quad \text{for } i = 1, 2, 3. \quad (2.1)$$

Here u_i is the fluid velocity in the x_i direction. This continuity equation means that the flow is divergence-free or solenoidal.

The conservation of momentum is based on Newton's second law, $F = ma$, which relates acceleration of fluid particles to the forces experienced by the fluid. Neglecting the gravity and body forces, the only remaining force is the stress tensor, τ_{ij} which is defined for a Newtonian fluid as

$$\tau_{ij} = -p\delta_{ij} + \mu \left(\frac{\partial u_i}{\partial x_j} + \frac{\partial u_j}{\partial x_i} \right), \quad \text{for } i, j = 1, 2, 3. \quad (2.2)$$

where μ is the dynamic viscosity and p is the pressure. The Kronecker delta, δ_{ij} is 1 if the variables are equal, and 0 otherwise. According to the momentum equation, the fluid accelerates due to the forces acting on the particle and it follows

$$\frac{\partial u_i}{\partial t} + \frac{\partial u_i u_j}{\partial x_j} = -\frac{1}{\rho} \frac{\partial p}{\partial x_i} + \nu \frac{\partial^2 u_i}{\partial x_j^2} \quad (2.3)$$

where $\nu = \mu/\rho$ is the kinematic viscosity.

This set of equations is called the Navier-Stokes equations and together with the continuity equation, they govern the flow field, no matter whether the flow is laminar or turbulent.

2.2 Direct Numerical Simulation

In nature, laminar flows are rather an exception, and most of the interesting flows in engineering applications are turbulent. Turbulent flow is three-dimensional, time dependent, has large Reynolds number (Re), includes a wide range of both time and length scales, and it is diffusive and dissipative. From the point of view of numerical simulations, the existence of a wide range of characteristic length and time scales is crucial, since for a successful simulation one should be able to capture all these scales.

A simulation that resolves all flow scales is called Direct Numerical Simulation (DNS). While DNS is not a feasible method for engineering problems due to the high computational cost, it is, however, a powerful research tool. From DNS results, almost any quantity can be evaluated, and once the numerical simulation is successful, the problem can be studied in more detail than experiment.

With the advent of massively parallel computers, DNS has been successfully applied to the study of the flow physics of turbulence [17] [18] [19] [20], active flow control and validation of the computational models. A thorough review of different applications of DNS is provided by Moin and Mahesh [21].

DNS solves the Navier-Stokes equations without any turbulence model. Therefore the whole range of spatial and temporal scales from the smallest to the largest scale of turbulence must be resolved. For the spatial scales, the resolution is related with computational mesh (grid). The smallest dissipative scales are called Kolmogorov scales, which is defined as $\eta = (\mu^3/\varepsilon)^{1/4}$, ε is rate of kinetic energy dissipation. The integral scale, L , contains most of the kinetic energy of the structures [22]. The smallest structures decrease with increasing Reynolds number and are proportional to $Re^{3/4}$. In a three-dimensional domain this yields $N^3 \approx Re^{9/4}$, where N is the number of grid points needed to resolve the smallest structures. The time scale is of the order of

$\sim Re^{3/4}$, therefore the total number of floating point operations required for the DNS are of the order of Re^3 .

DNS is an expensive tool and has some restrictions about computing capabilities. It must be stressed, that the objective of DNS is not to simulate real-life flows, but rather to use it as an academic research tool, allowing the study of flow physics and thus the development of improved turbulence models, which can then be used in commercial flow solvers.

2.3 Numerical Method, Geometry and Boundary Conditions

The DNS code used here, was developed by M.P. Simens [23] and J. Jimenez, and later modified by A.G. Gungor and M.P. Simens to introduce roughness and wake effects [8] [9].

The code solves the three-dimensional primitive-variable formulation of the incompressible Navier-Stokes equations in a three-dimensional rectangular volume. The three flow directions are the wall-normal, the streamwise, and the spanwise directions and velocity components are x, y, z and u, v, w , respectively. The code is written in Fortran and parallelized with Message Passing Interface (MPI).

The code uses the fractional-step method [24] [25] to solve the governing equations for the velocity and pressure fields. Fourier decomposition is used in the periodic spanwise direction, with compact finite difference [26] used in the aperiodic wall-normal and streamwise directions. The equations are discretized on a staggered grid. Uniform grids are used in x and z , with a non-uniform grid in y direction to cluster points in the near-wall region.

A three sub-step, semi-implicit low storage Runge-Kutta scheme [23], in which wall-normal second derivative terms use a Crank-Nicholson scheme to increase the time step, is used to evolve the equations in time. A full description of the numerical algorithm along with validation studies can be found in Simens *et al* [23].

In this thesis study the low pressure turbine blade is modeled as a flat plate with a pressure distribution similar to suction side of low pressure turbine blades. The flat plate model is chosen to match the experiment in [1], in which a flat plate is set in a

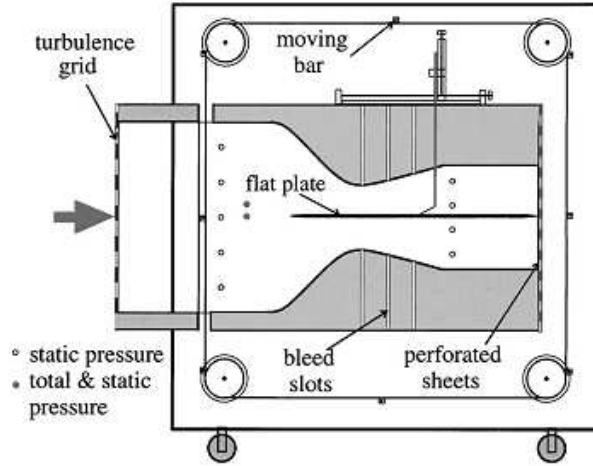


Figure 2.1: Schematic drawing of the experimental model of the wake forcing case [1].

convergent-divergent wind tunnel designed to reproduce the same pressure gradient as on the suction side of a T106C high-lift low-pressure turbine blade. The experimental set-up that is simulated here is given in Figure 2.1. The boundary conditions that model the experimental set-up in the numerical simulation is discussed here. Figure 2.2 shows the integration domain along with the instantaneous vorticity contours for all cases presented in this study.

No-slip boundary conditions are used at the bottom wall, for the streamwise, u , and spanwise, w , velocities, while the wall perpendicular component, v , is obtained using the impermeability condition. The laminar Hiemenz profile is prescribed at the inflow because this profile is the most similar profile to the experimental laminar profile. At the outflow, a convective boundary condition

$$\frac{\partial u}{\partial t} + U_c \frac{\partial u}{\partial x} = 0 \quad (2.4)$$

is applied at the exit of the computational box, with minor adjustments to the outflow streamwise velocity, U_c to enforce global mass conservation. The side boundaries are periodic.

To model the LPT blade on a flat plate a nearly constant suction velocity was imposed at the upper boundary. Therefore, the pressure distribution along the flat plate is representative of those in LPTs. The desired adverse pressure gradient is controlled by imposing a constant uniform wall-normal velocity at the top of the computational

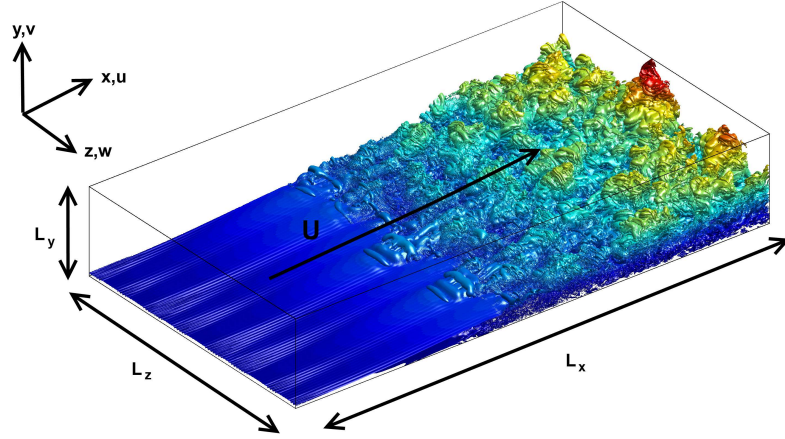


Figure 2.2: The numerical setup and the instantaneous visualization of the spanwise vorticity in an adverse pressure gradient turbulent boundary layer. The vortices are colored with the distance to the wall; blue (dark) near the wall, and red near the top. Flow is from bottom-left to top-right.

box. This APG can be calculated based on the free-stream velocity at the infinity as

$$U_{\infty}(x) = a_{APG}x + U_{\infty}(0), \quad a_{APG} = \frac{U_{\infty}(L_x) - U_{\infty,0}}{L_x} \approx -8.0. \quad (2.5)$$

where a_{APG} defines the strength of the APG, L_x is the domain length in the streamwise direction, $U_{\infty}(L_x)$ is the reference velocity at the end of the domain, and $U_{\infty,0}$ is the reference velocity at the inlet of the domain. Hence, the APG is a linear combination of the inflow and exit reference velocity.

At the upper boundary the u and w velocity components are determined by imposing $\partial u/\partial y = 0$ and $\partial w/\partial y = 0$. Over most of the domain these conditions are equivalent to zero-vorticity boundary conditions as v is constant.

The Reynolds number based on the inflow momentum thickness $\theta_0 = 0.268$ mm and the free stream velocity $U_{ref} = 6.3$ m/s is $Re_{\theta_0} = U_{ref}\theta_0/\nu \approx 110$. The momentum thickness, θ is defined as

$$\theta = \int_0^{\infty} \frac{u}{U_0} \left(1 - \frac{u}{U_0}\right) dy. \quad (2.6)$$

the integral of momentum defect across the boundary layer. The cost of DNS is highly related with the Reynolds number (for 3D domain $Re^{(9/4)}$), however, for our case the

Reynolds number based on the flat-plate length ($U_{ref}L_x/\nu = 170,000$) is low enough for an expensive DNS.

The simulation domain shown in Figure 2.2, $(L_x \times L_y \times L_z)/\theta_0 = 1640 \times 468 \times 123$ is discretized in $N_x \times N_y \times N_z = 1537 \times 301 \times 768$ collocation points and there are approximately 330 million grid points. All flow structures in the spatial and temporal space are resolved properly from the smallest scale (Kolmogorov scale) to the largest scale (integral scale). The grid resolution at the wall is $\Delta y^+ \approx 0.4$ (given in wall units), towards to boundary layer $\Delta y^+ \approx 2$ while $\Delta x^+ \approx \Delta z^+ \approx 2$ [9].

A variable time interval is used, determined by a constant CFL = 0.6 condition. The time interval is approximately 10.6 μs . So, even though the domain is small, the computations are intense. For example, the computational time for one wake passing is 7K CPU hours. The velocity field evolved for about 10 wake passing periods for the initial washout, and statistics are collected for another 10 periods, with a total cost of 140K CPU hours. It is similar for roughness cases.

2.3.1 Implementation of roughness

The surface roughness (trip wire) is implemented to the problem (Figure 2.3) using discrete the immersed boundary method (IBM) [27], [28]. This method modifies the governing equations with a forcing function and adds a source term to the N-S equation. This source term reproduces the effects of the boundary of the roughness element and acts as a velocity corrector for the grid points inside the immersed boundary [29].

The fluid is represented on an Eulerian coordinate and the roughness element is represented on a Lagrangian coordinate. The continuity equation **2.1** is defined in fluid domain Ω_f . The Newtonian, incompressible Navier-Stokes equations (momentum equation) eq. **2.3** are defined as,

$$\frac{\partial u_i}{\partial t} + \frac{\partial u_i u_j}{\partial x_j} = -\frac{1}{\rho} \frac{\partial p}{\partial x_i} + \nu \frac{\partial^2 u_i}{\partial x_j^2} + \frac{1}{\rho} f_i \quad (2.7)$$

where $f_i = f(x_i, t)$ is the source term (forcing function). Bandringa [29] explains the process as "In the discrete forcing approach, the governing equations **2.1** and **2.7** are

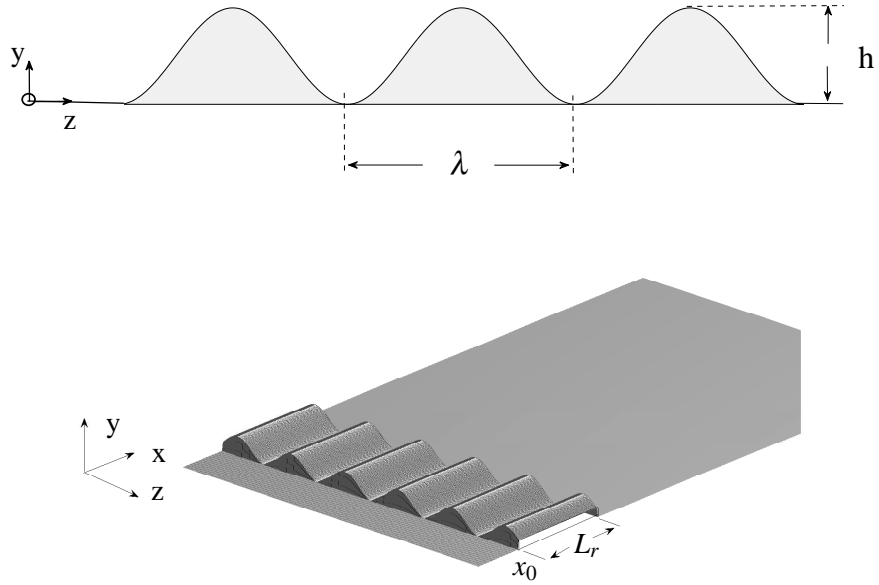


Figure 2.3: Schematic drawings of the cross-section (top) and three-dimensional (bottom) views of the discrete surface roughness.

discretized on a Cartesian grid neglecting the immersed boundary, it results in a set of discretized equations". The grid points in the neighborhood of the immersed boundary are computed using an interpolation scheme [8]. The details of the IBM are given in [27] and [28].

The trip wire roughness element is located upstream of the unforced separated position, $x_0 = 55\theta_0$. The roughness height, $h = 0.7\theta_0$ and wavelength, $\lambda = 126\theta_0$ are constant. The trip wire element changes like a sinusoidal function in the spanwise direction as shown in Figure 2.3. The surface length L_r , is changed in streamwise direction.

2.3.2 Implementation of wake forcing

Relative motion of the rows of the blades (moving part, rotors) makes the flow unsteady on constant part (stator) of the turbine. The combined effects of periodic disturbances (wake velocity defect and pressure fields) and random (wake turbulence) forces comes from rotor, effects the transition process in low pressure turbines [2]. Hence, wake passing period is an important parameter and controls the transition region on the rotor blade [9].

The wake behind the rotor is modeled as wake behind a circular cylinder. The fluctuations within in the wakes are neglected because detailed measurements of the incoming wakes were not available from the experiments. The turbulent mean wake velocity-profile that matches the experimental profile is given in [30] as

$$u_{wake}(\xi) = U_{ref} \frac{1}{4\sqrt{\pi}} \sqrt{\frac{U_{ref} c_d d_w}{\epsilon_0}} \left(\frac{x_w}{c_d d_w} \right)^{-\frac{1}{2}} \exp\left(-\frac{1}{4}\xi^2\right), \quad (2.8)$$

$$\frac{\epsilon_0}{U_{ref} c_d d_w} = 0.0222, \quad (2.9)$$

with

$$\xi = (y - U_w t) \sqrt{\frac{U_{ref}}{\epsilon_0 x_w}}, \quad t = \text{time}, \quad (2.10)$$

has been used. Here d_w is the diameter of the cylinder where $d_w/\theta_0 = 31$, $x_w = -1738\theta_0$ is the spatial distance to the cylinder to the plate, ξ is the dimensionless length scale, ϵ_0 is a constant in the wake-velocity profile, and c_d is the drag coefficient for a cylinder and it is approximately equals to unity. The wake profile, where the maximum wake deficit is $U_{wd} = 0.13U_{ref}$ and the mean wake half-width is $130\theta_0$, is shown in Figure 2.4.

The artificial wakes are assumed to be generated by a linear row of cylinders moving in the vertical direction with a speed of $U_w = -0.83U_{ref}$ as shown in Figure 2.5. Depending on the frequency of the wake, $1/\mathcal{T}$, where $\mathcal{T} = D_w/U_w$ is the period, D_w is the distance between the centerlines of the wakes and U_w is the speed of the wakes, there could be either one single wake or multiple wakes can be found on the inflow plane. A wake will be found in the computational domain if its centerline (y_c)

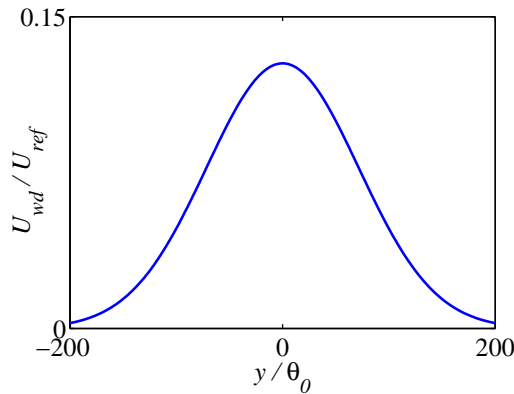


Figure 2.4: Wake velocity deficit profile respect to the free-stream velocity.

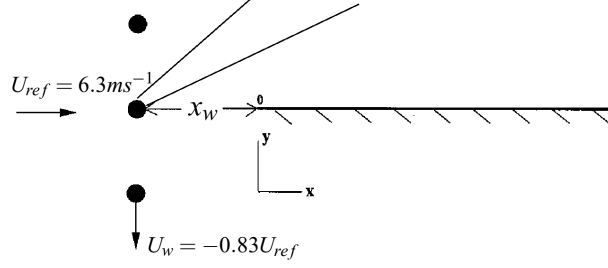


Figure 2.5: Schematic drawings of numerical model of the wake forcing case.

is located in the inflow plane. Therefore, the total number of wakes at any time is

$$\mathcal{N} = \frac{L_y}{|U_w| \mathcal{T}}. \quad (2.11)$$

The non-dimensional frequency based on the length of the plate and the reference velocity at the inlet defined as

$$St = \frac{fL_x}{U_{ref}} \quad (2.12)$$

is the Strouhal number where, $f = 0.83U_{ref}/D_w$ is the wake passing frequency. For the forcing frequencies considered here, St varies between 0.78 and 1.5. The low- St case that is investigated in this study, to be presented in chapter 4, is approximately of the order of the operating conditions of a low-pressure turbine.

Finally, at the inflow of the computational domain, the velocity components become

$$u(x=0, y, z) = U_h + u_{pb}(y, z) + U_h(u_{wake} \cos(U_w/U_{ref})), \quad (2.13)$$

$$v(x=0, y, z) = V_h + V_h(u_{wake} \sin(U_w/U_{ref})), \quad (2.14)$$

$$w(x=0, y, z) = 0, \quad (2.15)$$

where U_h and V_h denote the components of the Hiemenz profile. If no wakes are imposed, $u_{wake} = 0$. Note that a numerical problem arises at the bottom of the computational domain. The negative wake velocity at the lower boundary limits the no-slip boundary condition. Therefore, the wake velocity is multiplied by the Hiemenz profile in order to satisfy the no-slip boundary condition at the lower wall. Furthermore, steady three-dimensional perturbations, u_{pb} are also explicitly added at the inflow for transition to occur since otherwise spectral codes along the span, like the one used here, would remain strictly two dimensional [23].

3. THE EFFECT OF ROUGHNESS LENGTH ON THE CONTROL OF SEPARATED BOUNDARY LAYERS

3.1 Introduction

Understanding the underlying mechanism for roughness-induced transition will lead to several control strategies, which is particularly important for aerodynamic and turbo-machinery applications where the early transition to turbulence leads to a significant reduction of the laminar separation bubble in the separated region and hence, the pressure loss.

Earlier experimental and numerical studies indicate that the laminar turbulent transition mechanism is strongly affected by the presence of localized roughness. The two-dimensional roughness element accelerates the transition process by tripping the boundary layer. The effect of a three-dimensional tripwire (the tripwire has a varying height along the spanwise direction) on boundary layers subject to adverse pressure gradient has been discussed in [8]. In that article the influence of height, wave-number and distance on the separation bubble were discussed. However, the influence the length of the tripwire on the transition mechanism was not discussed. Although no influence is expected, we will show that indeed the length of the tripwire can be an important parameter to control the transition mechanism.

The purpose of this study is to present new results on the control of strong APG boundary layers, and to study the effect of a tripwire on the transition dynamics and the separation bubble for the APG boundary layer flow simulated especially in this study.

This chapter begins with a description of the numerical methodology employed to undertake the DNS of the APG boundary layer flow. This is followed by a discussion of the results, beginning with a visual assessment of the flow field to identify the different structures that emerge behind the roughness in various regions of the flow, and followed by a more in-depth presentation of their role in controlling the separation

bubble and the mean flow parameters. The chapter concludes with a brief summary of the main results.

3.2 Numerical Details

A direct numerical simulation of a boundary layer with a streamwise pressure distribution similar to those encountered on the suction side of turbine blades is performed. The Reynolds number based on inlet momentum thickness and maximum streamwise velocity at the inlet, is $Re_\theta = 110$.

In order to study the effect of the roughness length on the transition dynamics, the streamwise length L_r of the roughness, drawn schematically in Figure 2.3, is varied while the wavelength and height of the roughness are held constant at $\lambda = 126\theta_0$ and $h = 0.7\theta_0$ respectively. For all configurations roughness is located slightly downstream of the inflow, $x_0 = 55\theta_0$ where the flow is still laminar and attached.

The parameters of the numerical experiments are summarized in table 3.1. The case $\mathcal{RW}0$ is a base uncontrolled (without roughness) simulation by [23], and $\mathcal{R}3d$ is the short roughness simulation by [8] used for comparison. The new case simulated especially in this study, where the roughness length is almost three times longer than the $\mathcal{R}3d$ case will be denoted as $\mathcal{R}3dL$ hereon. The streamwise extent of the bubble L_b is defined as $L_b = x_r - x_s$ and L_{b0} is the bubble length of the uncontrolled case, $\mathcal{RW}0$.

The pressure gradient parameter at separation point defined as

$$\Lambda_s = \frac{\theta_s^2}{\nu} \frac{dU_e}{dx} \Big|_s, \quad (3.1)$$

lies in the range $-0.171 < \Lambda_s < -0.083$ as suggested in [31] for laminar separation. Reynolds number based on the momentum thickness at the separation point θ_s , $Re_{\theta_s} = \frac{U_{ref}\theta_s}{\nu}$ is approximately 160 for the rough cases. These parameters indicate that the separation occurs in the laminar region for all cases.

Statistical averages are performed over the homogeneous spanwise direction and time, with the total averaging time is $T_{ave} = 11000\theta_0/U_0$, which is equivalent to about 7 flow-through times.

Table 3.1: Parameters of the roughness simulations and characteristics of the separated region. The momentum thickness, θ_0 , is measured at the inflow. x_s and x_r represent the streamwise location of the separation and reattachment point, respectively.

Case	L_r/θ_0	x_s/θ_0	x_r/θ_0	Re_{θ_s}	Λ_s	L_b/L_{b_0}
$\mathcal{RW}0$	-	215	700	160	-0.089	1.0
$\mathcal{R}3d$	36	285	550	164	-0.113	0.46
$\mathcal{R}3dL$	109	268	550	160	-0.105	0.53

3.3 Results

This section begins with a visual assessment of the flow field to identify the different structures that emerge behind the roughness in various regions of the flow, and followed by a more in-depth presentation of their role in controlling the separation bubble and the mean flow parameters.

3.3.1 Flow structures in transition region

It has been observed that the uncontrolled flow (without roughness) is initially laminar, separates, transitions within the separation bubble, reattaches as a result of the transition, and finally develops into an attached turbulent adverse-pressure-gradient [8]. The streamwise evolution of the three-dimensional structures of the uncontrolled flow is presented in Figure 2.2. The roughness element located upstream of the bubble does not cause the flow to transition, but it is responsible for generating perturbations that hasten the reattachment, x_r of the separation bubble as presented in Table 3.1 for all cases.

The coherent structures are visualized through vorticity and the second-invariant of the velocity gradient tensor [32] contours.

The vorticity is defined as the curl of the velocity vector,

$$\omega_i = \varepsilon_{ijk} \frac{\partial u_k}{\partial x_j}, \quad \varepsilon = \begin{cases} 1, & \text{if } i, j, k \text{ are all different and in cyclic order} \\ -1, & \text{if } i, j, k \text{ are all different and in acyclic order} \\ 0, & \text{otherwise} \end{cases} \quad (3.2)$$

and the components of the vorticity in Cartesian coordinates are

$$\omega_x = \frac{\partial w}{\partial y} - \frac{\partial v}{\partial z}, \quad \omega_y = \frac{\partial u}{\partial z} - \frac{\partial w}{\partial x}, \quad \omega_z = \frac{\partial v}{\partial x} - \frac{\partial u}{\partial y}. \quad (3.3)$$

The second-invariant of the velocity gradient tensor is defined as,

$$Q = \frac{1}{2} [P^2 - S_{ij}S_{ji} - R_{ij}R_{ji}], \quad (3.4)$$

$$P = A_{ii}, \quad S_{ij} = \frac{1}{2} (A_{ij}A_{ji} + A_{ji}A_{ij}), \quad R_{ij} = \frac{1}{2} (A_{ij}A_{ji} - A_{ji}A_{ij}), \quad (3.5)$$

where $A_{ij} = \partial u_i / \partial x_j$ is the velocity gradient, S_{ij} is the rate-of-strain tensor, R_{ij} is the rate of the rotation tensor, and P is the first invariant which is zero for the incompressible flow due to continuity.

A representation of the separated shear layer and vortical structures that develop in the rough cases are visualized in Figure 3.1. Isosurfaces of the second-invariant of the velocity gradient tensor are shown in Figure 3.2. Because of the APG, an inflectional point is created in streamwise direction. Because of the inflection point, the flow is unstable due to inviscid Kelvin-Helmholtz (KH) instability. As the KH waves convect downstream, it perturbs the separated shear layer until the shear layer rolls-up into discrete two-dimensional spanwise vortices that shed from the shear layer and convect downstream [11], [33].

Figure 3.1 shows a uniform shear layer up to the transition point, after which three-dimensional fluctuations are observed followed by a rapid breakdown of the shear layer into smaller vortices. The interaction of these 2D vortices with the disturbances generated by the roughness lying underneath amplifies the spanwise waviness of the KH vortex until it breaks down into smaller three-dimensional flow structures [34].

Watmuff [35] has observed hairpin-like structures in the separated shear layer, which provide a mechanism for the wall-normal exchange of momentum. These hairpin-like structures are also apparent in the transition and reattachment region of the separated boundary layer as shown in figures 3.2 for $\mathcal{R}3d$ and $\mathcal{R}3dL$ cases, respectively.

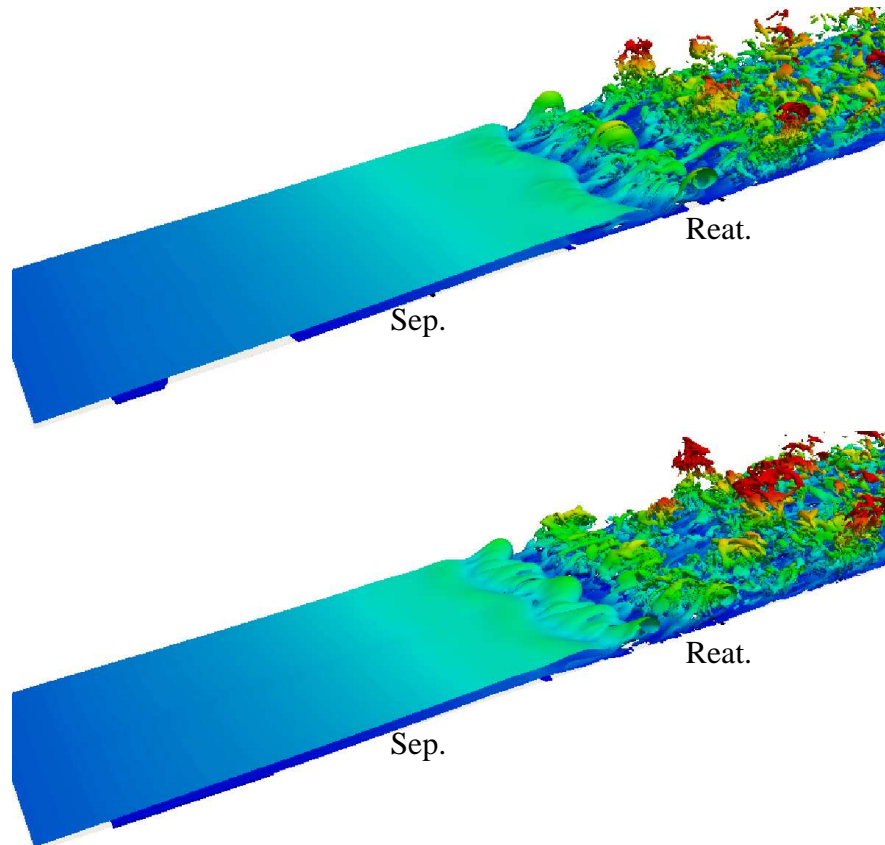


Figure 3.1: Instantaneous snapshots of spanwise vorticity contours. Top: $\mathcal{R}3d$; bottom: $\mathcal{R}3dL$. Flow is from bottom to top right, and the box is $650\theta_0 \times 120\theta_0 \times 260\theta_0$. The isosurface is colored by the distance to the wall, from $y/\theta_0 = 0$ for the deepest blue, to $y/\theta_0 = 50$ for the brightest red. Note roughness height $h = 0.7\theta_0$

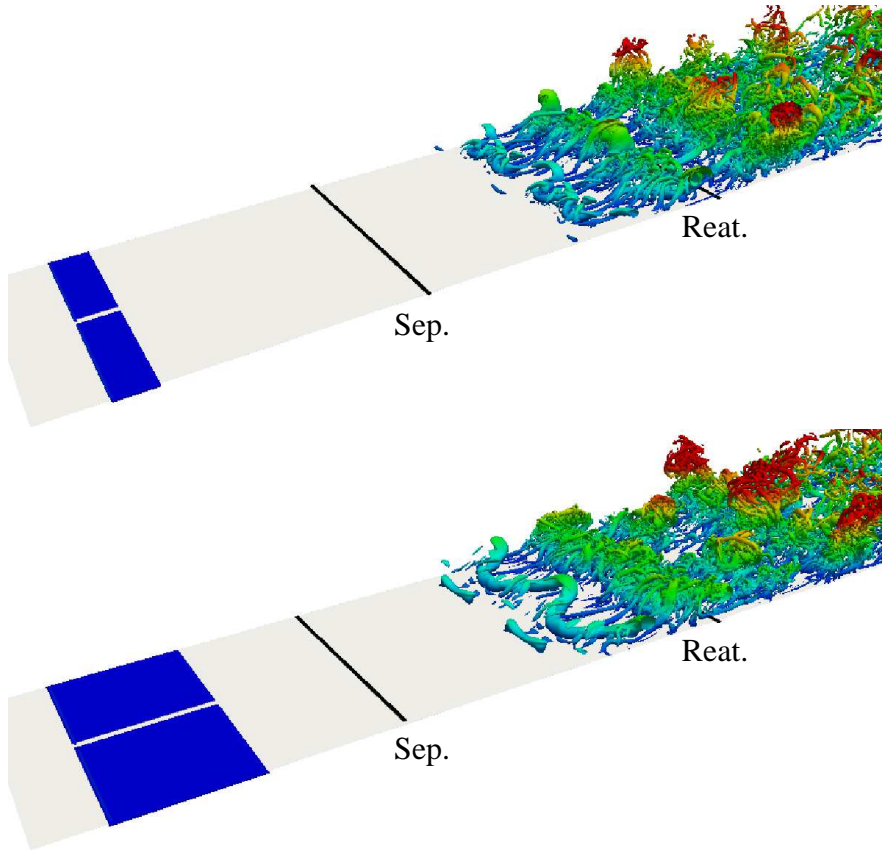


Figure 3.2: Instantaneous snapshots of second-invariant of the velocity gradient tensor. Top: $\mathcal{R}3d$; bottom: $\mathcal{R}3dL$. Flow is from bottom to top right, and the box is $650\theta_0 \times 120\theta_0 \times 260\theta_0$. The isosurface is colored by the distance to the wall, from $y/\theta_0 = 0$ for the deepest blue, to $y/\theta_0 = 50$ for the brightest red. Note roughness height $h = 0.7\theta_0$

The streamwise vorticity for the cases $\mathcal{R}3d$ and $\mathcal{R}3dL$ on xz plane at a wall normal distance of $y/\theta_0 = 5$ is shown in Figure 3.3. The vorticity is normalized with its maximum. The dark red contours show positive vorticity and the dark blue one shows negative value of the vorticity component, ω_x . The vertical lines represent the locations $x/\theta_0 = 60, 84, 132$ and 226 which correspond to just after the roughness, in the middle of the roughness, after the roughness, and before the separation location for $\mathcal{R}3d$ case, and just after roughness, inside the roughness, just before the end of the roughness, and before separation location for $\mathcal{R}3dL$ case, respectively. These locations are used in the same order in Figure 3.4.

The streaky structures are clearly seen from these figures. The streaks, as defined in [36], are "the perturbations elongated in streamwise direction consisting of negative/positive streamwise velocity perturbations, which induce localized regions of decelerated/accelerated flow". Streamwise vorticity or spanwise-dependent vertical motion in shear flows is the main source of the streaky structures and lift-up effect [36]. The streaks are responsible for maintaining turbulence by mixing positive and negative velocity with each other. The streaks are generally seen after the transition and elongated in streamwise direction. For our study, streaks are generated from the valley location and peak at the location of the roughness element. Streaks come from valley location or openings, live longer than the peak location of the roughness element (Figure 3.5). Away from the wall, the strength of the streaks are increasing.

The streamwise evolution of the streamwise vorticity is depicted in Figure 3.4. The arrows are the cross flow (v, w) velocity vectors, and the magenta lines are the zero contours of the streamwise velocity. The left column is $\mathcal{R}3d$ and the right column is $\mathcal{R}3dL$ case. The red contours shows positive streamwise vorticity and blue contours shows the negative vorticity. The '0' point represents the center location of the roughness element openings. The flow comes from the openings generate the three-dimensional instability. Moreover, streaks and coherent structures are generated from these openings as mentioned earlier. The streamwise vorticity structures leave from the wall and continue to evolve along the streamwise direction. Due to this effect, momentum transfer enhances. It is interesting to note that, initially for the case $\mathcal{R}3dL$,

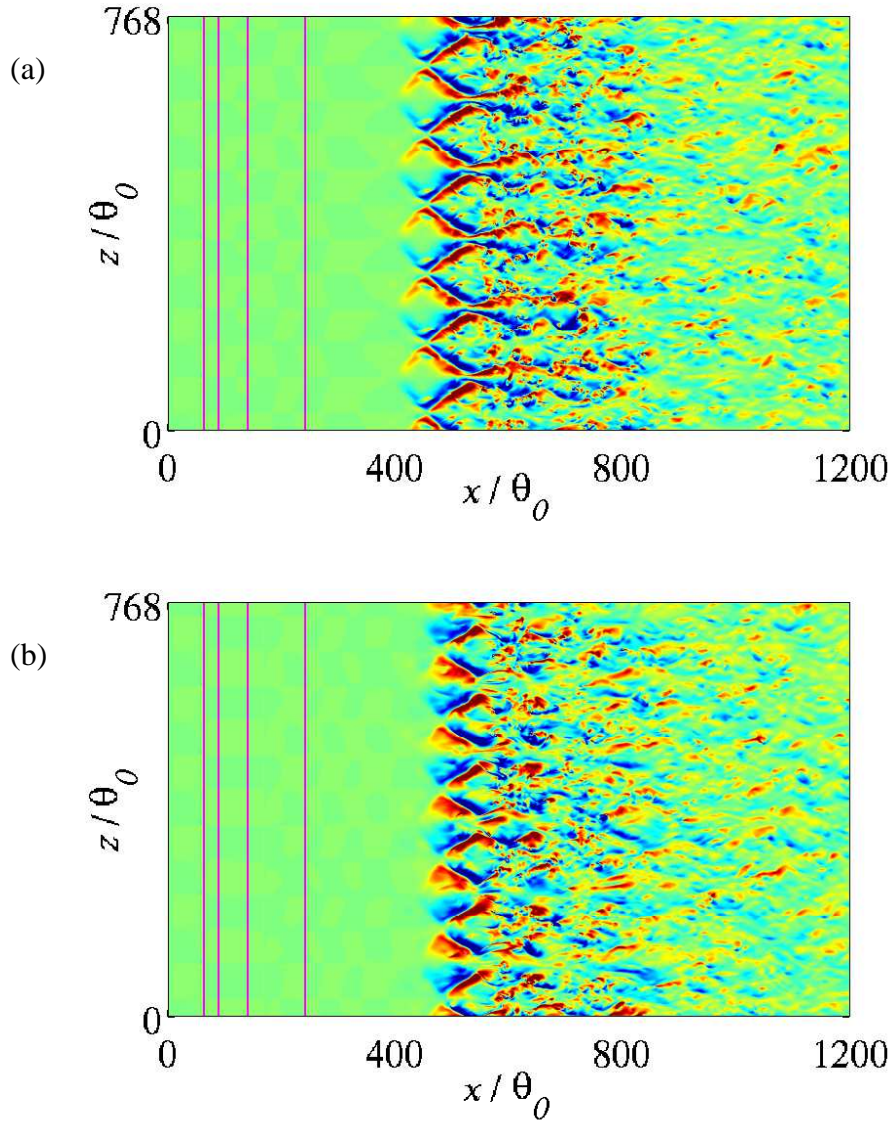


Figure 3.3: Streamwise vorticity contours, (a) $\mathcal{R}3d$ and (b) $\mathcal{R}3dL$ on xz plane and $y/\theta_0 = 5$. $0 < \omega_x/\omega_x|_{max} < 1$. The magenta lines represents the locations of $x/\theta_0 = 60, 84, 132$ and 226 .

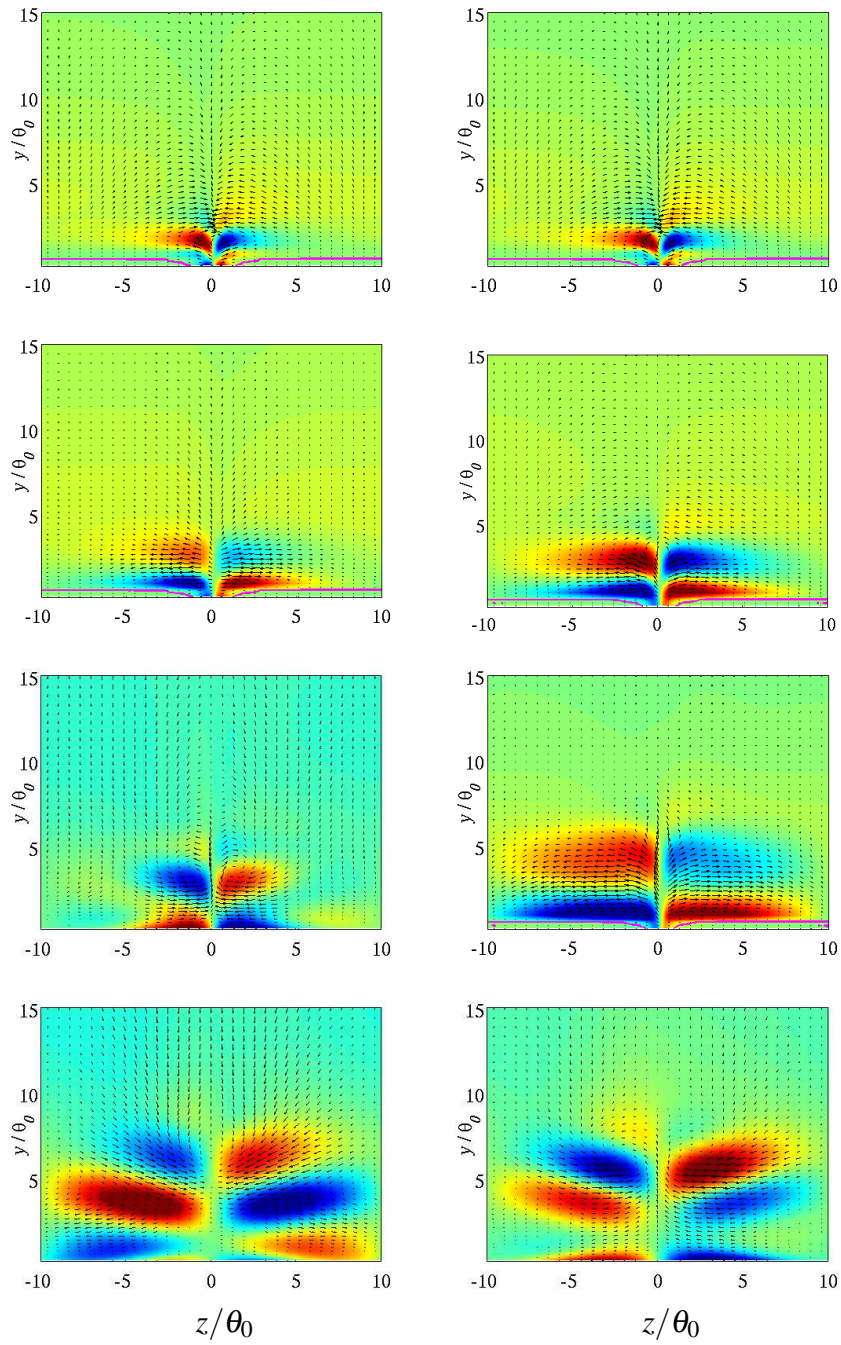


Figure 3.4: Streamwise vorticity contours (shaded contours) of the surface trip of the cases $\mathcal{R}3d$ and $\mathcal{R}3dL$ on yz plane at different x locations. $0 < \omega_x / \omega_{x_{max}} < 1$. The arrows are the cross flow (v, w) velocity vectors, and the magenta line is the zero contour of the streamwise velocity. Left column: $\mathcal{R}3d$, Right column: $\mathcal{R}3dL$. From top to bottom, $x/\theta_0 = 60, 84, 132$ and 226 .

streamwise vorticity structures move to higher points in wall normal direction and also spread in spanwise direction compare to the $\mathcal{R}3d$ case.

Figures 3.5 and 3.6 illustrate the instantaneous streamwise velocity contours for the $\mathcal{R}3d$ and $\mathcal{R}3dL$ cases in a xz plane. The upper Figure shows the flow inside the roughness element, $y/\theta_0 = 0.3$ and the bottom Figure shows the flow outside the roughness element, $y/\theta_0 = 20$ but still inside the boundary layer. The length of the roughness elements are clearly seen from the upper figures. It can be clearly seen from this Figure, for all cases flow accelerates while passing through from the openings, which causes an increase to the momentum transfer between the layers inside the boundary layer. An increase in the momentum transfer causes an increase in the energy transfer from mean velocity to velocity fluctuations. So, the velocity difference between the layers are getting equalized, shear forces (skin friction drag) are increased, but the pressure drag is decreased slightly in this region. Note that the magnitude of the pressure drag is highly related to the size of the laminar separation bubble.

The flow oscillates in spanwise direction like a waveform, as presented in Figures 3.5 and 3.6. Since the roughness is imposed on the problem as a sinusoidal function in the spanwise direction (Figure 2.3), the effect comes from this sinusoidal roughness element continues to influence to the flow structures up to the fully turbulent region. After that region, the flow loses its history.

Results indicate that the three-dimensional roughness located upstream of the bubble does not cause the flow to transition immediately, but is responsible for generating perturbations that hasten the reattachment of the separation bubble. The flow after the trip element is still laminar, and perturbations due to the trip element hardly grow until the bubble starts to form. It is seen that transition to turbulence starts approximately at the same streamwise location in both cases. However, the transition scenario is different in both cases. Whereas the $\mathcal{R}3d$ case shows an oblique wave the $\mathcal{R}3dL$ case shows more of a mushroom shape. For the long roughness case the transition develops in a very distinct way compared to the $\mathcal{R}3d$ case. This is somewhat surprising, because one would expect that the wavenumber would be the most important parameter for the transition scenario. The way in which this wavenumber is imposed on the flow was always assumed to be of little importance.

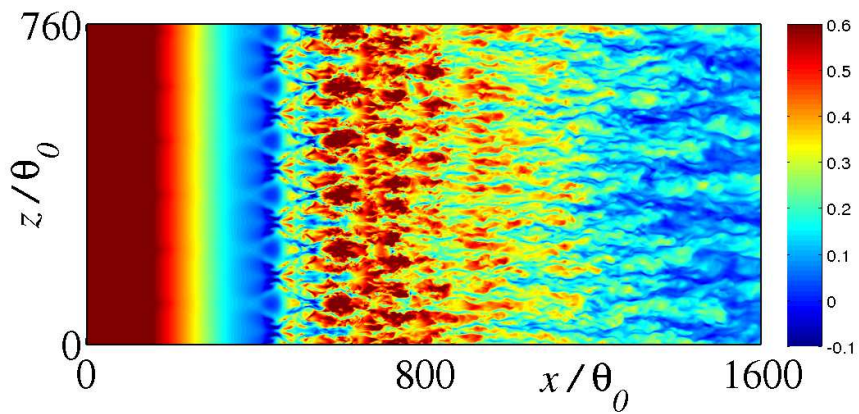
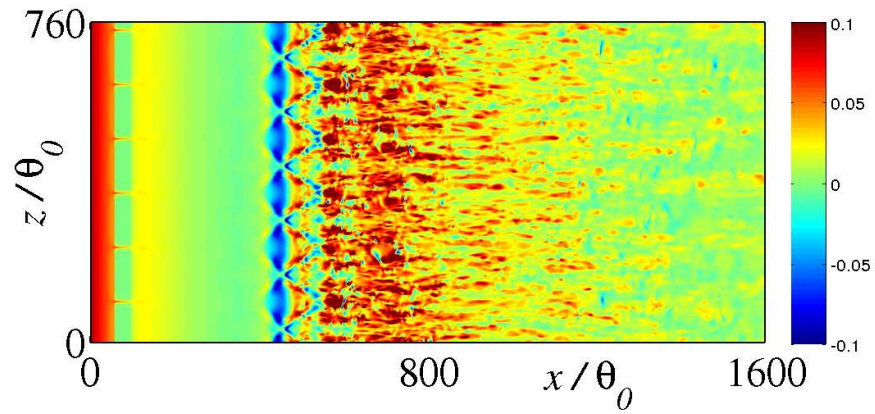


Figure 3.5: Streamwise velocity contours in xz plane of the cases $\mathcal{R}3d$. Dark red contours after the roughness element are positive streaks and blue contours are negative streaks. Top: inside the roughness ($y/\theta_0 = 0.3$), Bottom: outside the roughness ($y/\theta_0 = 20$)

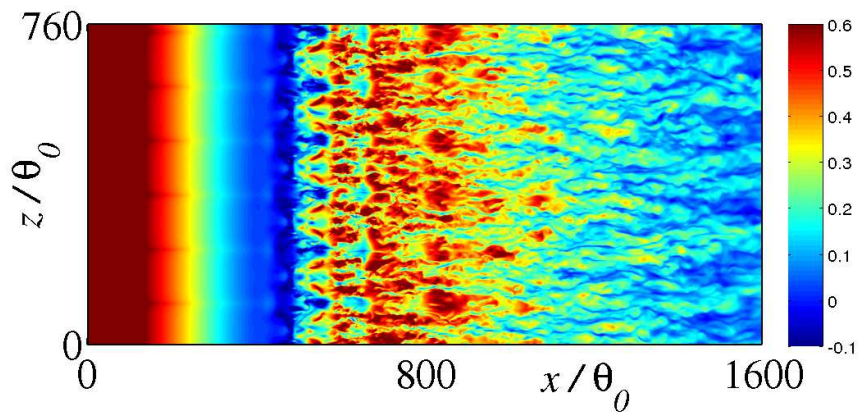
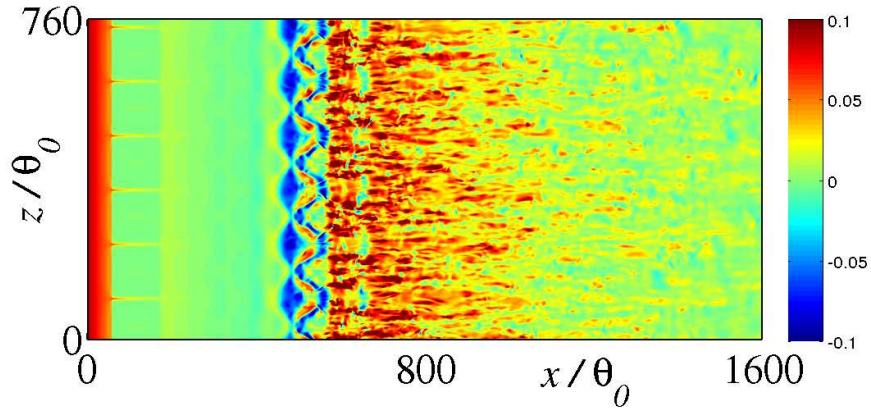


Figure 3.6: Streamwise velocity contours in xz plane of the cases $\mathcal{R}3dL$. Dark red contours after the roughness element are positive streaks and blue contours are negative streaks. Top: inside the roughness ($y/\theta_0 = 0.3$), Bottom: outside the roughness ($y/\theta_0 = 20$)

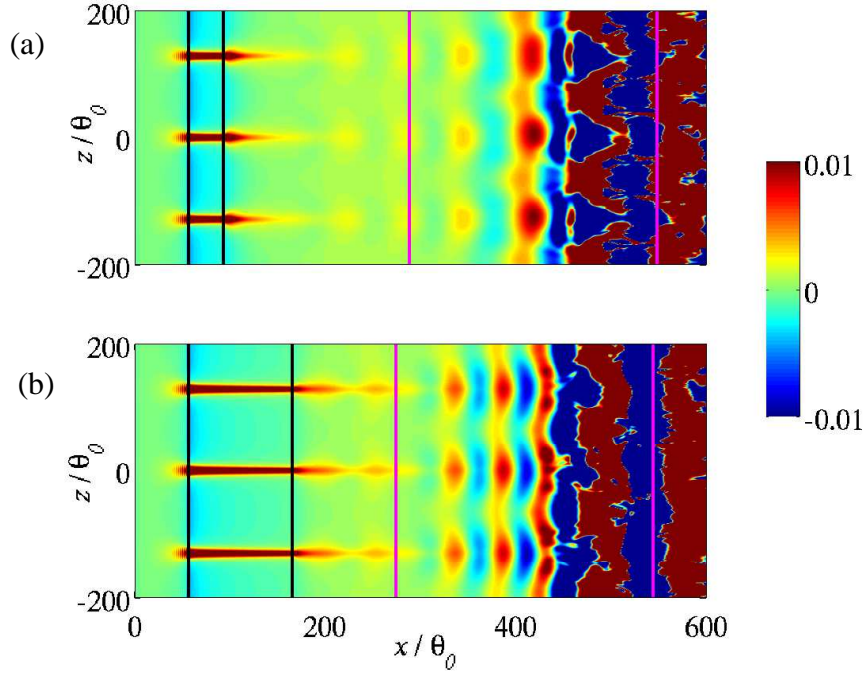


Figure 3.7: Streamwise evolution of the u'/U_e in a wall-parallel at $y/\theta_0 = 0.5$. (a) $\mathcal{R}3d$; (b) $\mathcal{R}3dL$. Black and magenta lines denote the streamwise extent of the roughness and separation bubble, respectively.

In order to elucidate the reason for this difference we looked at the streamwise velocity fluctuation, u' defined as,

$$u'_i = u_i - \langle U_i \rangle \quad (3.6)$$

where, $\langle U \rangle$ is the mean velocity component. Figure 3.7 depicts the contour of the u' and identifies the high wave-number disturbances upstream of the separation. The streaks in this Figure represent disturbance paths that are generated as a result of the roughness pattern. This Figure clearly shows that the difference between the two lengths is due to an increased amplitude of the streak.

Figure 3.8 compares the u' and $d\langle U \rangle/dy$ profiles at streamwise locations of $x/\theta_0 = 50, 165$, and 200 . The first streamwise location is just before the roughness. At $x/\theta_0 = 50$ both $\mathcal{R}3d$ and $\mathcal{R}3dL$ show similar distributions in the boundary layer. Due to the acceleration of the flow in the openings of the roughness, the streamwise intensities are amplified. The boundary layer at $x/\theta_0 = 200$ is still attached though on the verge of separation. The $\mathcal{R}3d$ case shows a fuller profile at this point.

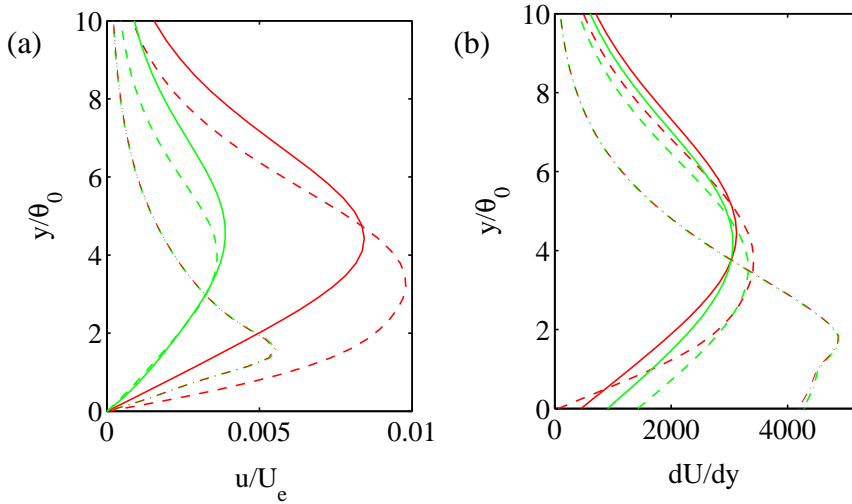


Figure 3.8: (a) u'/U_e and (b) $d\langle U \rangle/dy$. --- : $x/\theta_0 = 50$; -.-.- : $x/\theta_0 = 165$; — : $x/\theta_0 = 200$. Green: $\mathcal{R}3d$, Red: $\mathcal{R}3dL$.

The underlying transitional mechanisms due to short and long roughness are distinctly different. Figures 3.9 and 3.10 illustrate the time-series evolution of the "transitional" structures. A three-dimensional disturbance with a fixed spanwise wavelength λ is induced due to the roughness. In fact, it is shown that such a disturbance generates very small vortices. These vortices interact non-linearly with the large amplitude KH vortices of the separated shear layer, producing an oblique 3D vortices with the spanwise wavelength λ . The vortices exhibit "peaks" and "valleys", i.e., regions of enhanced and reduced wave amplitude [37] in spanwise direction, half a spanwise wavelength $\lambda/2$ apart, as shown in Figures 3.9 and 3.10. At the peak location, the breakdown of the instantaneous high-shear layer vortices into smaller vortices is observed for both cases. A qualitatively similar formation is observed for the $\mathcal{R}3dL$ case. However, due to more intense and larger amplitudes of the disturbances the vortices undergo a more rapid breakdown. For the short roughness case a sub-harmonic instability appears to result in a streamwise pairing of the shed vortices and a doubling of their streamwise spacing, similar to that observed in free shear layers [38]. The streamwise growth of the wave packet via the generation of multiple hairpin vortices is clearly seen for the $\mathcal{R}3d$ case.

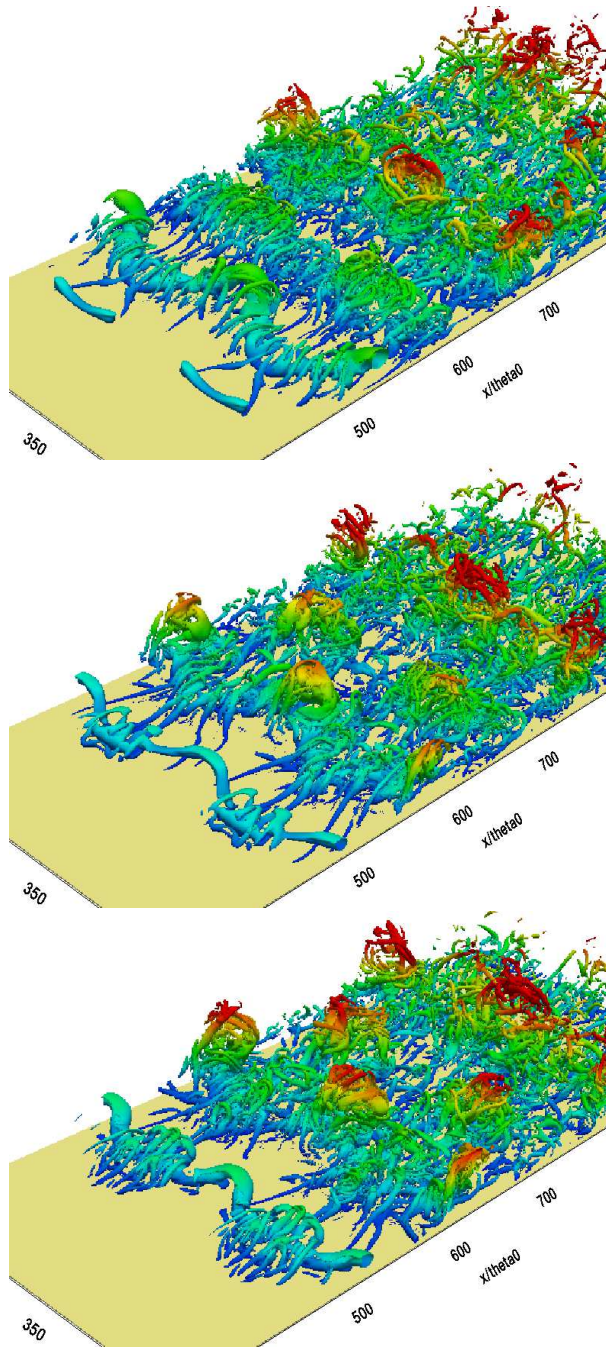


Figure 3.9: Evolution of the transitional structures of the $\mathcal{R}3d$ case at three different time instances t_1 , t_2 and t_3 . Isosurface of the second-invariant of the velocity gradient tensor colored by the distance to the wall, from $y/\theta_0 = 0$ for the deepest blue, to $y/\theta_0 = 50$ for the brightest red. Flow is from bottom left to top right.

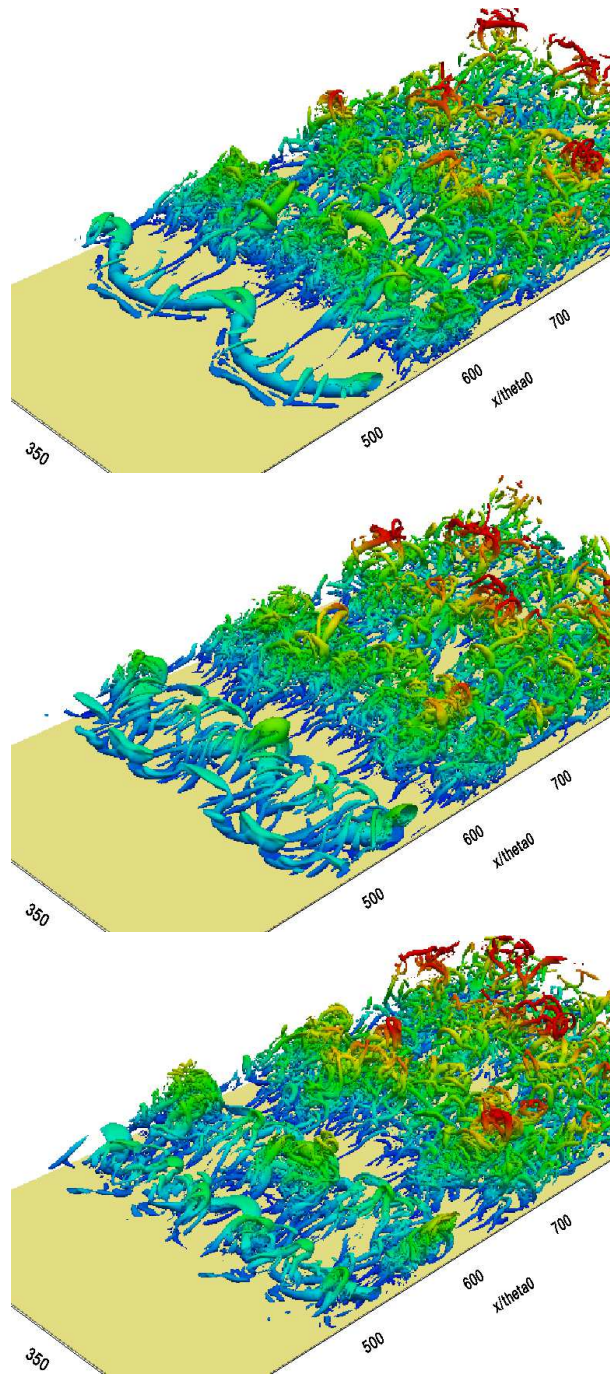


Figure 3.10: Evolution of the transitional structures of the $\mathcal{R}3dL$ case at three different time instances t_1 , t_2 and t_3 . Isosurface of the second-invariant of the velocity gradient tensor colored by the distance to the wall, from $y/\theta_0 = 0$ for the deepest blue, to $y/\theta_0 = 50$ for the brightest red. Flow is from bottom left to top right.

3.3.2 Mean flow parameters

The streamwise evolution of the mean flow characteristics are presented in the following section for both short and long roughness and are compared with the smooth case of [39]. Table 3.1 also summarizes the characteristics of the separation region.

The mean spanwise vorticity distribution in the lower half of the domain is shown in Figure 3.11. The time-averaged separated region ($U(x, y = 0, z) < 0$) and the boundary layer growth are also indicated in the same Figure with thick solid lines. The separated region, shown by thick solid lines in the figures, becomes quite thin and short in the rough cases. Due to the effect of roughness not only the reattachment point moves upstream but also the separation point moves downstream. The more significant difference is observed in the wall-normal extension of the separation bubble. The roughness element distorts the boundary layer development, resulting in a significant decrease in the growth of the boundary layer thickness. The white dashed lines shown, indicate the inflection points in the velocity profile. The profiles have an inflection point imposed by the APG, which is the precursor of the separation and transition [40]. Flow fluctuations originate at the inflection points of the separated shear layer formed by the separation bubble.

In order to assess the nature of the turbulence activity around the separation region, the streamwise variation of the root-mean-square (rms), $\sqrt{\langle u^2 \rangle}$ velocity fluctuations are depicted in Figure 3.12. The rms value indicates information about the turbulent intensity, higher value of rms means higher level of turbulence. The maximum value of the rms are seen just behind the transition region for all cases except for the u_{rms} of the case $\mathcal{RW}0$. The roughness elements give the flow, initially two-dimensional perturbations, and trigger the inviscid Kelvin-Helmholtz instability that is responsible for the breakdown to turbulence. Kelvin-Helmholtz instability is characterized by the formation of large, two-dimensional vortices in the separated shear layer. The large amplitude fluctuations seen in Figure 3.12 are due to the regular shedding of these vortical structures. The growth of these fluctuations in the initial part of the separated region is slow, whereas they grow much faster close to reattachment. This

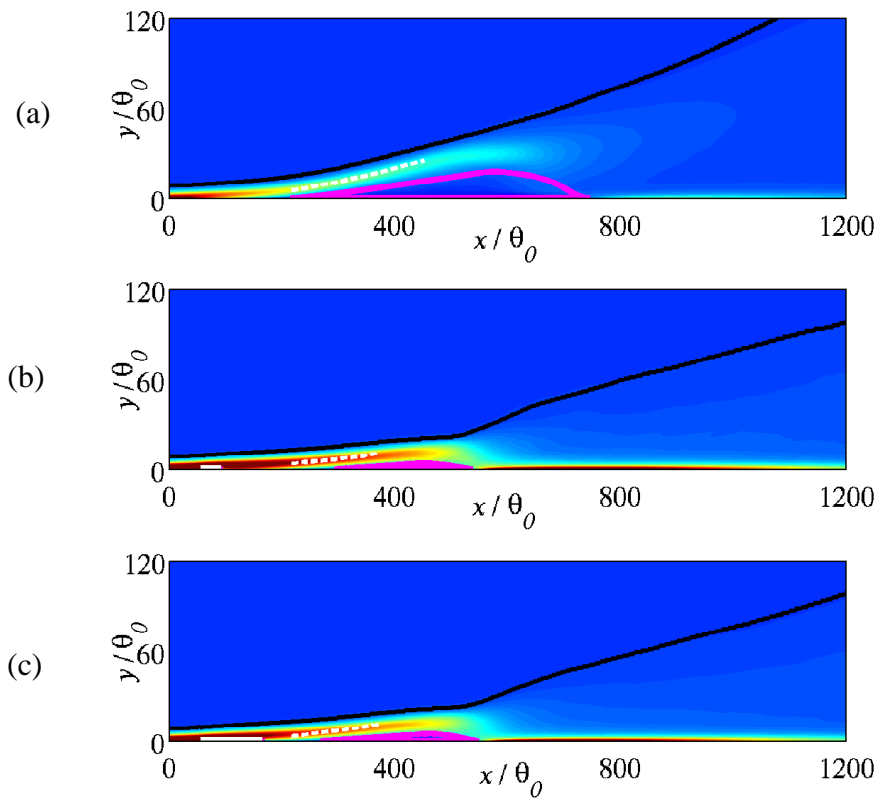


Figure 3.11: Mean spanwise vorticity contours, $0 < \omega_z / \omega_{z_{max}} < 1$ (a) $\mathcal{RW}0$, (b) $\mathcal{R}3d$ and (c) $\mathcal{R}3dL$. Black line: boundary layer thickness, white dashed line: inflection point, magenta line: zero contours of streamwise velocity.

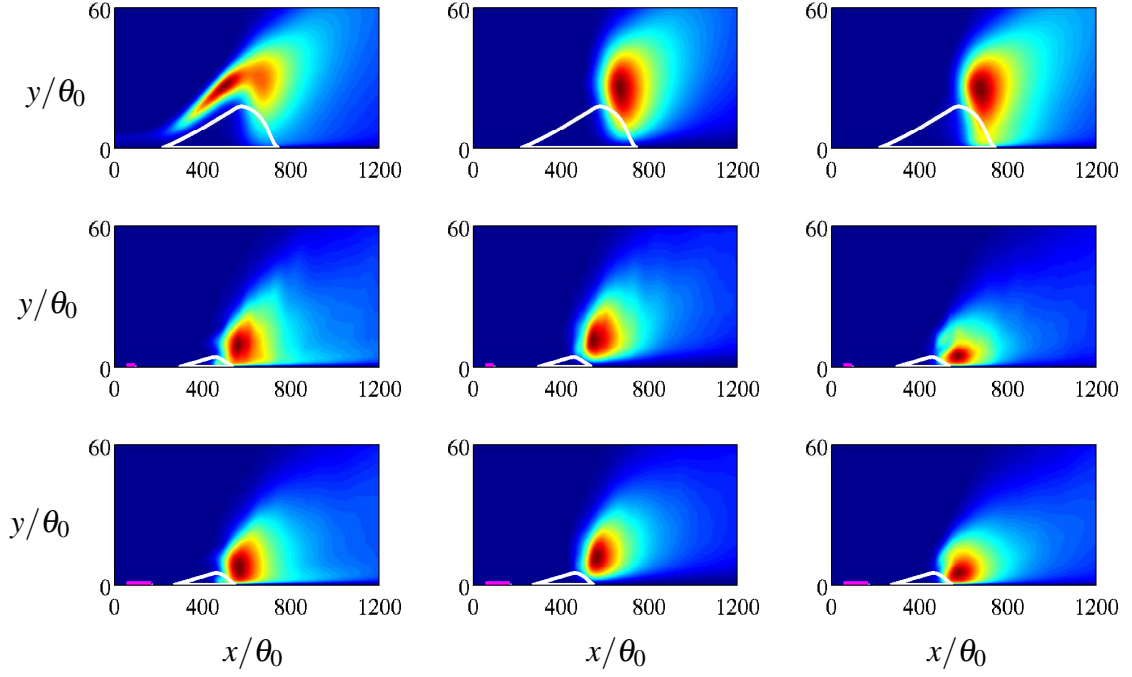


Figure 3.12: Root mean square contours of the velocity fluctuations in xy plane of the cases $\mathcal{R}W0$, $\mathcal{R}3d$ and $\mathcal{R}3dL$. From left to right: u_{rms} , v_{rms} , and w_{rms} ; from top to bottom: $\mathcal{R}W0$, $\mathcal{R}3d$, and $\mathcal{R}3dL$. The rms values are normalized with the maximum value of each other, $0 < u_{i,rms}/u_{i,rms_{max}} < 1$. The magenta lines represent the length of the roughness element.

sudden growth of the fluctuations triggers a slowdown of the bubble growth due to the turbulent energy diffusion, and reattachment occurs. The reattachment of the flow is accompanied by an overall maximum in the turbulent intensity. This intensity decreases slowly downstream, while the peak location is shifted outward from the reattachment point to the end of the solution domain.

The streamwise evolution of the mean flow integral parameters are presented in Figure 3.13 for both short and long roughness and are compared with the smooth case of [39]. In these figures black, green and red lines show the smooth, $\mathcal{R}3d$ and $\mathcal{R}3dL$ cases, respectively. The solid lines correspond to the separated region ($U(x, y = 0, z) < 0$) and vertical dashed lines denote the streamwise extent of the roughness field.

Figure 3.13(a) shows the evolution of the skin friction coefficient,

$$C_f = \frac{\tau_w}{\frac{1}{2}\rho U_{ref}^2}, \quad \tau_w = \mu \frac{\partial \langle U \rangle}{\partial y} \Big|_{y=0} \quad (3.7)$$

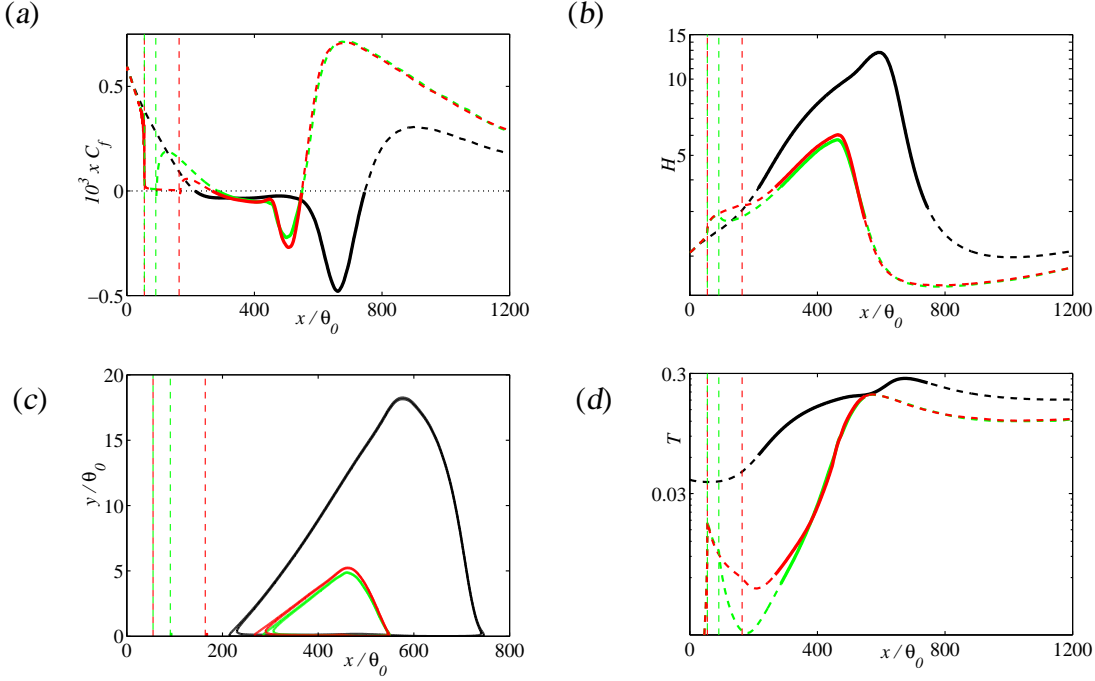


Figure 3.13: Streamwise evolution of the (a) skin friction coefficient; (b) shape factor; (c) separation bubble; (d) maximum turbulent intensity. Black: Smooth, Green: $R3d$, Red: $R3dL$. — : separated flow, $C_f < 0$, and ---- : attached flow, $C_f > 0$. Vertical dashed lines denote the streamwise extent of the roughness field.

which gives a quantitative measure of the length of the separated region which has significantly decreased for the rough cases. It is apparent that due to the amplified disturbances upstream and accelerated flow through the openings of the roughness, the separation point moves slightly downstream while transition and reattachment are promoted significantly [8]. The results, however, show that the longer roughness is less effective for separation delay.

To assess the nature of the flow within the boundary layer, the streamwise variation of the shape factor,

$$H = \delta^*/\theta \quad (3.8)$$

is depicted in Figure 3.13(b) in semi-log plot. For the roughness cases, the shape factor, and hence the profile loss, is reduced significantly compared to the smooth case. The vertical displacement of the boundary layer is squeezed, indicating that the boundary layer is accelerated downstream of the roughness. This acceleration is specifically apparent for the short case which moves the separation point slightly downstream as compared to long case (see also Table 3.1).

The streamwise variation of the separation bubble which is determined by the zero-contour of the streamwise velocity, is given in Figure 3.13(c). The roughness pattern strongly affects the separated region, which is shortened from both sides and lowered compared to the smooth case. The flow accelerates while passing through the openings of the roughness. This acceleration causes an increase in momentum transfer and delays the separation. Also roughness moves the reattachment point upstream, due to faster transition and hence increased wall-normal mixing. The wall-normal extension of the separation bubble decreased considerably by 80% from smooth to rough case.

The shape and extent of the separation bubble depend largely on the transition mechanism. The evolution of the maximum turbulent kinetic energy which is defined as

$$T(x) = \max_y \left(\sqrt{\frac{1}{3} (\langle u'u' \rangle + \langle v'v' \rangle + \langle w'w' \rangle)} / U_\infty(x) \right) \quad (3.9)$$

complements these observations, as shown in Figure 3.13(d). Note that steady three-dimensional perturbations exist at the inflow for the smooth case for transition to occur. The presence of surface roughness generated additional disturbances in the boundary layer, and hence, changes the initial disturbance level before amplification begins. The linear growth of the disturbances is observed soon after the separation, while the non-linear growth sets in approximately at the maximum bubble height.

Alam and Sandham [41] observed that the viscous Tollmien-Schlichting (TS) instability of the reversed flow along the wall may dominate the inviscid instability of the separated shear layer when the reversed flow velocity exceeds about 20% of the local free-stream velocity. In both cases studied here, the reverse-flow remained less than 8% of the local free stream velocity, indicating that, if instability exists, it is inviscid rather than viscous.

The ratio of the wall-normal location of the maximum turbulent intensity, y_{max} , to the inflection point, y_{inflec} , is shown in Figure 3.14. The location of the disturbance growth relative to the inflection point indicates that the disturbances are not amplified through a viscous (TS) instability mode, in which the maximum amplification is located close to the wall but through a inviscid KH instability mechanism of the separated shear layer [42]. By using shorter roughness pattern, a significant attenuation of the

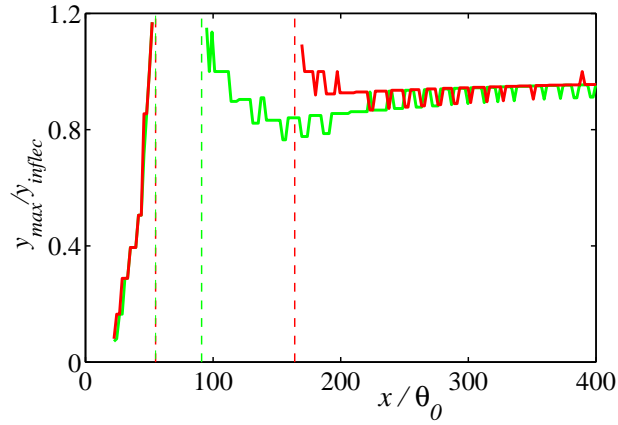


Figure 3.14: Streamwise evolution of the y_{max}/y_{inflec} . Green: $\mathcal{R}3d$, Red: $\mathcal{R}3dL$. Vertical dashed lines denote the streamwise extent of the roughness field.

KH-wave amplitude is observed as shown in Figure 3.13(d) which is followed by the sudden growth of the streamwise fluctuations due to inviscid instability in the separated shear layer. While the initial disturbance amplitudes are different, the $\mathcal{R}3dL$ induced disturbances are not enough to cause a significant difference in the mean flow. So, the mean flow parameters are very similar for the short, $\mathcal{R}3d$ and long, $\mathcal{R}3dL$ cases.

3.4 Summary

In this chapter we focus on two aspects of the roughness induced flow: details of the flow in the transition region are presented first and subsequently some insight is provided into the separation and mean flow parameters.

Results indicate that transition to turbulence is triggered by the three-dimensional perturbations generated through the openings of the roughness element. Streaky structures which are responsible for the mixing process in the boundary layer are generated from the openings of the roughness element. These streaks that represent the disturbance path as a result of the roughness pattern, interact nonlinearly with KH vortices of the separated shear layer, resulting in an increase in the local disturbance level. As a result of that, the separation is delayed, transition and reattachment locations move upstream. Hence, the laminar separation bubble size significantly reduced compared to the base case.

Difference between the short and long roughness is due to an increased amplitude of the streaks. However, disturbances come from the long rough case are not strong enough to cause a difference in mean flow parameters compared to the short rough case. Increasing roughness length is less effective, mean flow characteristics are roughly same with short rough case.

4. WAKE AND ROUGHNESS EFFECTS ON THE CONTROL OF BOUNDARY LAYERS

4.1 Introduction

Rotor-stator interaction plays a vital role in the design of a turbomachinery. The wake passing period, distance between rotor and stator, and some other parameters affect efficiency, noise, fuel consumption of the turbo-engine. Since, LPT blades are exposed to high loadings during operation and for other environmental and mechanical reasons, the surfaces of the blades are subject to some deformation. Also, it is well-known that surface roughness is used as a flow control element. So, the combined effect of surface roughness and large-scale wake forcing are important to investigate.

This chapter is organized as follows: After describing the numerical setup we discuss in detail the combined effect of wake passing frequency and discrete surface roughness on the separated flow. First, instantaneous and mean flow characteristics are discussed. Then, Strouhal number effect (non-dimensional wake passing frequency) is studied for different wake passing periods ($St = 0.78$ and $St = 1.55$). The space-time evolution of the separated region and phase-averaged variation of the skin friction coefficient are compared with each other. The chapter ends with a short summary.

4.2 Numerical Details

The LPT blade is modeled as a flat plate with a proper pressure gradient and the wake behind the rotor is modeled as a wake behind circular cylinder. A detailed description on the implementation of the wake forcing is given in chapter 2.

The main characteristics of the flow and the separated region are summarized in Tables 4.1 and 4.2, respectively. The wake parameter $St = \frac{fL_x}{U_{ref}}$, is the Strouhal number based on the wake passing frequency, the length of the plate and the reference velocity at the inlet. The case $\mathcal{RW}0$ is a base uncontrolled simulation by [23], used for

Table 4.1: Parameters of the adverse-pressure-gradient boundary layer simulations, L_b/L_{b0} is the ratio of the length of the separated region to length of the unforced separation region.

Case	St	Re_θ	L_b/L_{b0}
$\mathcal{RW}0$	0	110-1600	1.0
$\mathcal{R}3d$	0	110-1022	0.512
$\mathcal{W}St155$	1.55	110-980	0.3810
$\mathcal{R}3d\mathcal{W}St1.55$	1.55	110-895	0.3619
$\mathcal{R}3d\mathcal{W}St0.78$	0.78	110-915	0.4162

Table 4.2: Characteristics of the separated region. The parameters, x_s , x_{tr} and x_r are calculated at the separation, transition and reattachment locations respect to inflow momentum thickness, θ_0 .

Case	Re_{θ_s}	Λ_s	x_s/θ_0	x_{tr}/θ_0	x_r/θ_0
$\mathcal{RW}0$	161	-0.089	214	657	742
$\mathcal{R}3d$	164	-0.113	285	-	550
$\mathcal{W}St155$	167	-0.118	295	-	490
$\mathcal{R}3d\mathcal{W}St0.78$	165	-0.0892	296	478	516
$\mathcal{R}3d\mathcal{W}St1.55$	165	-0.1168	303	456	495

comparison. $\mathcal{R}3d$ is the three-dimensional roughness simulation. $\mathcal{W}St155$ is the wake forcing simulation with $St = 1.55$. $\mathcal{R}3d\mathcal{W}St0.78$ and $\mathcal{R}3d\mathcal{W}St1.55$ are wake forcing simulations using three-dimensional roughness element, with $St = 0.78$ and $St = 1.55$, respectively. In this study, we use the short tripwire element whose properties are the same as $\mathcal{R}3d$ case, presented in Chapter 3.

The Reynolds number, based on the momentum thickness, Re_θ which gives a measure of aerodynamic loss arising from the boundary layer, is presented in Table 4.1. The growth of θ , as a result of the APG and the separation bubble, is the reason that Re_θ increases. Note that in the base case, $\mathcal{RW}0$, Re_θ at the end of the simulation domain is 1600. It is evident that the momentum thickness, hence Re_θ is significantly decreased for controlled cases.

The conditions at the separation points presented in Table 4.2 lie within the range of values observed in previous studies. The Reynolds number based on the momentum thickness at the separation point Re_{θ_s} is about 165 and it is insensitive to the control method. This value is consistent with the ones obtained by [4], where Re_{θ_s} ranged from 136 to 432 for laminar separation. For all cases, the value of the pressure gradient

parameter at the separation point, $\Lambda_s = \frac{\theta_s^2}{\nu} \frac{dU_e}{dx} \Big|_s$ [31] is consistent with prior studies; [43] found $-0.171 < \Lambda_s < -0.083$ for the onset of laminar separation. Separation x_s , reattachment x_r and transition x_{tr} locations with respect to inflow momentum thickness are also presented in Table 4.2.

The velocity field evolved for about 10 wake passing periods for the initial washout, and statistics are collected for another 10 periods, with a total cost of 140K CPU hours per simulation.

4.3 Results

4.3.1 Flow description

Figure 4.1 presents the instantaneous streamwise velocity fluctuations, u' for the separate and combined effects of surface trip and wake passing. The time-averaged separated region is also indicated in the same figure with thick solid lines.

The uncontrolled flow, $\mathcal{RW}0$ shown in Figure 4.1(a) is initially laminar, separates, transitions within the separation bubble, reattaches due to the transition, and develops into an attached turbulent APG boundary layer as mentioned before.

The distributed surface roughness, case $\mathcal{R}3d$ increases the turbulent fluctuations in the turbulent boundary layer and it shifts the laminar-turbulent transition to some upstream position, as shown in Figure 4.1(b).

The unsteady forcing, case $\mathcal{W}St155$, in which all the turbulent fluctuations except for the mean velocity defect are neglected, triggers the transition of the separated shear layer, modifies the separated region, and results in a shorter and lower separation bubble (Figure 4.1(c)).

The combined effect of both the unsteady forcing and discrete roughness, case $\mathcal{R}3d\mathcal{W}St1.55$, exerts different effects at the flow, as presented in Figure 4.1(d). Both effects decrease the boundary layer losses and hence the drag forces by reducing the separation length and height of the laminar bubble.

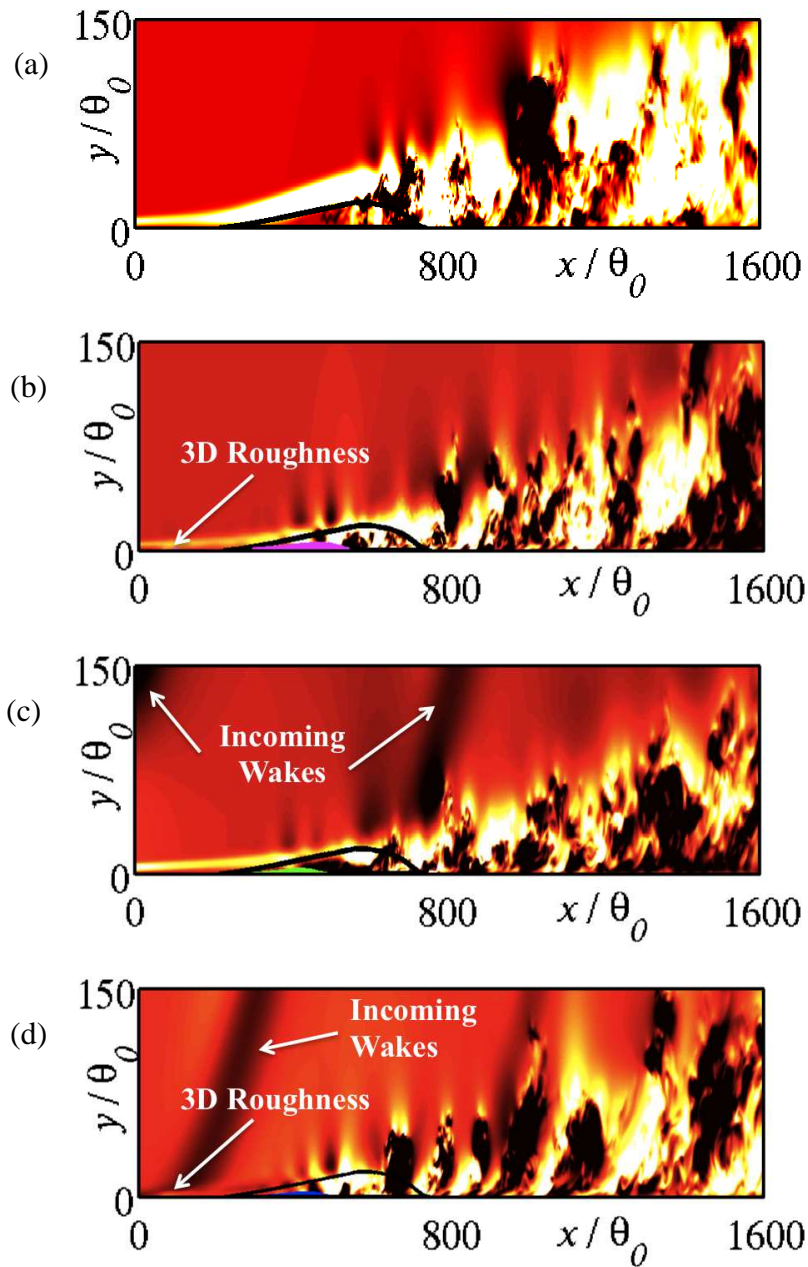


Figure 4.1: Streamwise velocity fluctuation (shaded contours) and the zero contour of the streamwise velocity (lines). The contours are $(-0.05, 0.1)$ of the reference velocity. (a) $RW0$; (b) $R3d$; (c) $W St1.55$; (d) $R3dW St1.55$.

4.3.2 Mean flow statistics

Figure 4.2 shows the streamwise development of the mean flow properties of the rough and wake simulation, $\mathcal{R}3d\mathcal{W} St1.55$. It is compared with the APG simulation in [23], the wake simulation in [9], and the three-dimensional roughness simulation in [8].

The time-averaged separation region is depicted in Figure 4.2(a). In the base case, $\mathcal{R}W0$, a large unsteady separation bubble due to the adverse pressure gradient starts about $x/\theta_0 = 214$ and reattaches at $x/\theta_0 = 742$. The separated region becomes quite thin and short in the controlled cases. The more significant decrease is observed in the wall-normal extension of the separation bubble. Not only the reattachment point moves upstream, but also the separation point moves downstream while the height of the separation bubble is reduced. This is due to the mean flow deformation by the wake transport of the mean momentum towards the near-wall region in the case of the large-scale wake forcing, and due to the accelerated flow in the openings of the three-dimensional roughness element.

The separate and combined effects of surface trip and wake passing on the time averaged shape factor H and the skin friction coefficient C_f are compared in Figures 4.2(b) and 4.2(c), respectively. It can be seen that the unperturbed case results in a longer region of separated flow with a flat skin friction distribution and higher values of the shape factor. The large-scale forcing and roughness alter the boundary layer development, resulting in a significant decrease in the overall displacement of the separation bubble and length.

The streamwise variation of the maximum turbulent intensity, T is shown in Figure 4.2(d). For the controlled cases, the growth of the disturbances in the initial part of the separated region is slow, whereas they grow much faster in the downstream part of the separated region. This sudden growth of the streamwise fluctuations triggers a slowdown of bubble growth due to turbulent energy diffusion and is responsible for the increase in the skin friction.

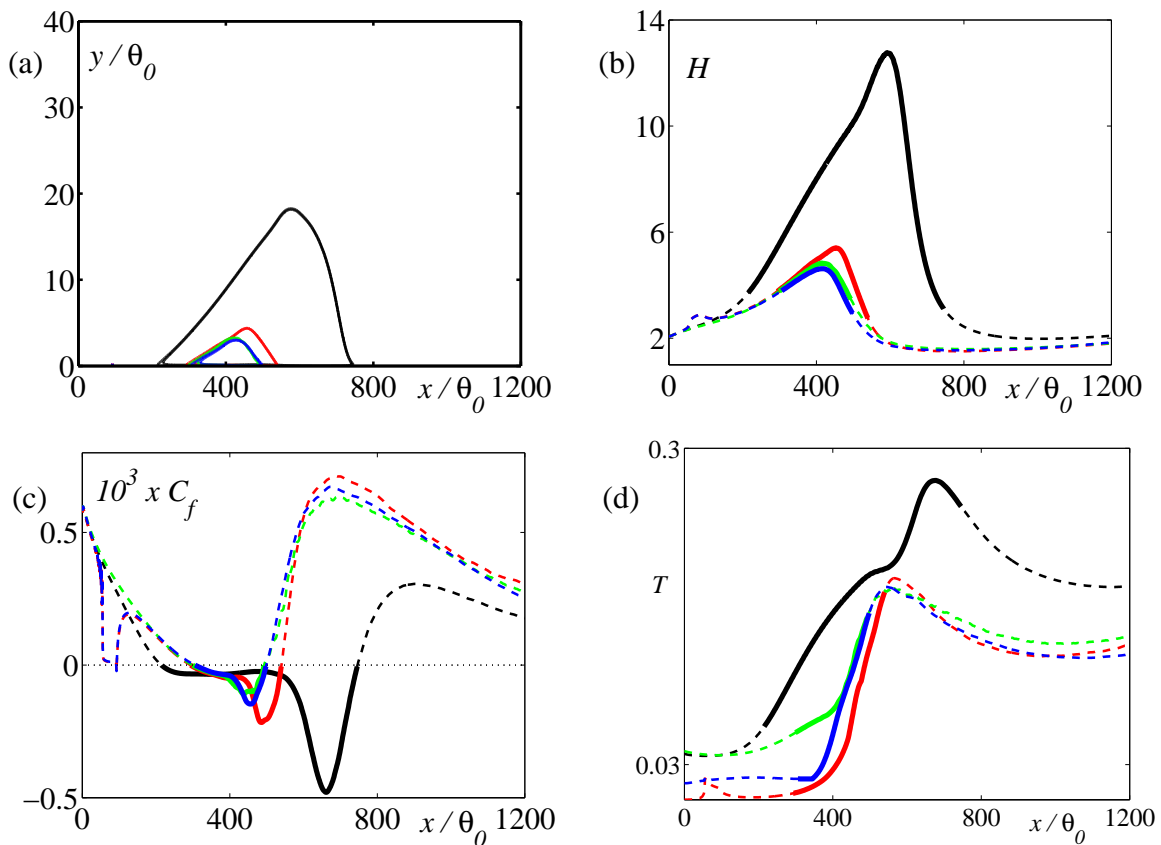


Figure 4.2: The individual and combined effects of surface trip and wake passing on the mean flow statistics. (a) Zero contour of the streamwise velocity, indicates the location of the separation bubble; (b) Shape factor; (c) Skin friction coefficient; (d) Maximum turbulent intensity. Black: $\mathcal{R}W 0$, Red: $\mathcal{R}3d$, Green: $\mathcal{W} St 1.55$, Blue: $\mathcal{R}3d\mathcal{W} St 1.55$.

The turbulent kinetic energy contours shown in Figure 4.3 provides a clear view of the turbulent activity around the separated region. The time-averaged separation region and the boundary layer thickness development are also indicated in the same plot with thick solid lines. The symbols shown indicate the inflection points in the velocity profile. The profiles have an inflection point imposed by the APG, which is the precursor of the boundary layer separation. Flow fluctuations originate on the line of inflection points in the velocity profile. The position of the maximum turbulent kinetic energy approximately matches with the position of the inflection points up to the maximum height of the separation point. This can be explained by the fact that the large shear near the point of inflection enhances the energy transfer from the mean flow to the fluctuations.

Note the levels of the turbulent kinetic energy in Figure 4.3. For the base case, the 2D instabilities grow in the separated shear layer that is located relatively away from the surface. In this case, it is the 2D instability accompanied by the inviscid Kelvin–Helmholtz instability that is responsible for the breakdown to turbulence [9]. The Kelvin–Helmholtz instability is characterized by the formation of large two-dimensional vortices in the separated shear layer. The large amplitude fluctuations seen in Figure 4.3 are likely due to the regular shedding of these vortical structures.

The wakes and roughness elements give the flow, initially two-dimensional perturbations. Individual studies on the effect of wakes [9] and roughness [8] show that both modify the spatial development of the laminar boundary layer by promoting the transition. And their combined effect is clearly seen in Figure 4.3(d) from the boundary layer thickness lines and Figure 4.2(d) (see the peak points of maximum turbulent kinetic energy in the figure). In the transition region the perturbations become three-dimensional. For the controlled cases, the shear layer is located relatively close to the surface, causing a significant effect of wall-damping on the shear layer and this results in lower intensities. For all cases, the shear layer spreading in the reattachment region and the development of high velocity gradients near the wall in the turbulent region are clear. The comparison between the individual influence of wakes and roughness on the separation indicates that the transition of the separated boundary

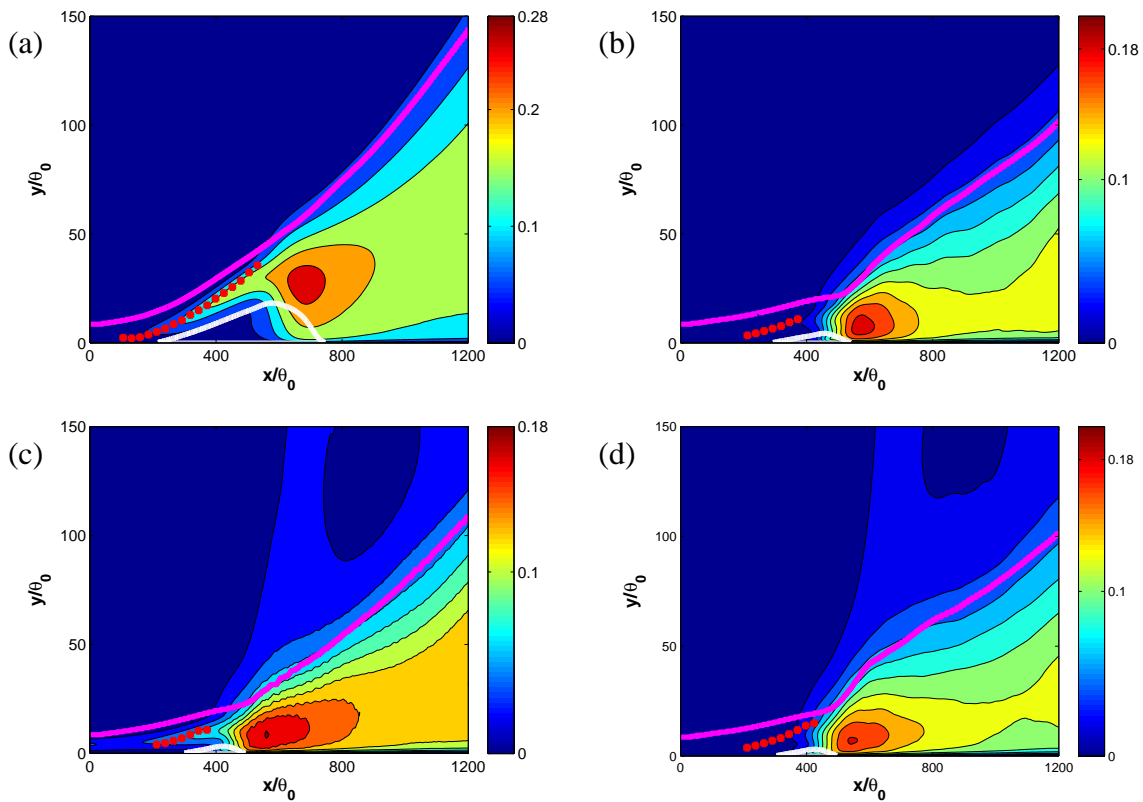


Figure 4.3: Turbulent kinetic energy contours (shaded contours), the boundary layer thickness (magenta lines), inflectional points (red symbols) and the zero contour of the streamwise velocity (white lines). The contours are nondimensionalized by the reference velocity. (a) $\mathcal{R}W0$; (b) $\mathcal{R}3d$; (c) $\mathcal{W} St1.55$; (d) $\mathcal{R}3d\mathcal{W} St1.55$.

layer with wakes occur almost at the same streamwise location as that induced by the roughness element. This indicates that the unsteady transition process and the growth rate of the disturbances are independent of the control mechanism. Furthermore, it is found that the mean flow statistics show almost similar trends for the unsteady smooth and rough cases.

4.3.3 Strouhal number effect

In the previous section, it is found that the effect of the roughness is negligible compared with the effect of wakes when the wake passing frequency, St is 1.55. In order to investigate the effect of wake forcing frequency, we extend these studies to a lower wake passing frequency. Here, we study the space-time development of $\mathcal{R}3dWSt0.78$ and $\mathcal{R}3dWSt1.55$ cases, presented in Table 4.1.

The space-time evolution of the separated region is shown in Figure 4.4. The negative wall-shear stress, depicted as black regions in the figure shows the separated region. The time axis is normalized with the wake passing period. Both numerical experiments have a separated region whose size changes periodically due to the influence of incoming wakes and surface roughness. Both studies show vortices originating at the top of the separated region. The wake impact and roughness effect modify the separation bubble and induces roll-up vortices. The signature of these roll-up vortex does not appear immediately downstream of the separation onset location, which suggests that the vortex can only form when the separated shear layer is at a certain distance from the surface. These roll-up vortices convect downstream at about half of the local free-stream velocity, similar to other experimental [2] and numerical studies [9].

For the lower wake passing period considered in the $\mathcal{R}3dWSt0.78$ case and shown in Figure 4.4(a), there is only one wake in the numerical domain. As the wake impacts the separated region, the separation bubble becomes unstable causing an increase in the level of mixing, which significantly reduces the separated region in size. After the wake passes the separated region again increases in size before it is impacted by the next wake. While for the high wake passing period case $\mathcal{R}3dWSt1.55$, there are two wakes in the numerical domain, see Figure 4.4(b). They are separated by a

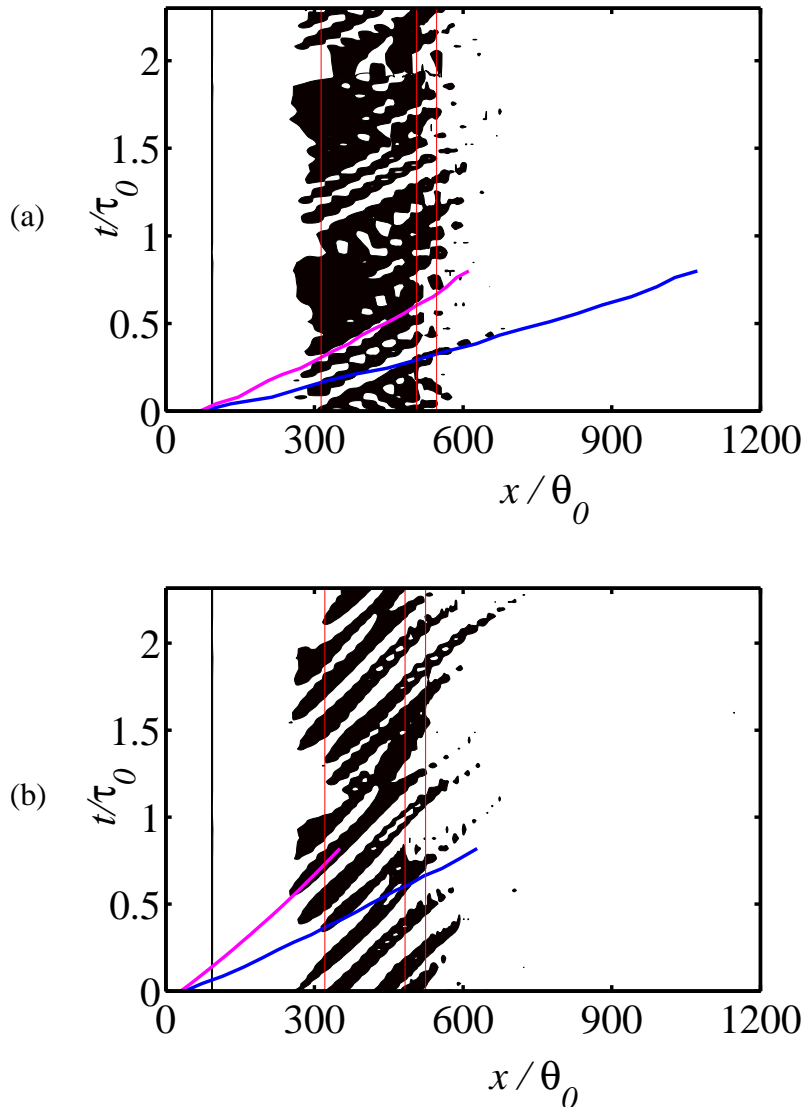


Figure 4.4: The development of the negative wall shear stress as a function of space and time. Top: $\mathcal{R}3dWSt0.78$; bottom: $\mathcal{R}3dWSt1.55$. The blue line traces the wake center and the magenta one waves generated by the wake. The propagation speed of these waves is $0.45U_e$. The vertical lines mark roughness, separation, transition, and reattachment points of the time averaged bubble.

distance of $x/\theta_0 = 920$. Between these two wakes there is not enough time for the bubble to regenerate itself. Furthermore, the roughness introduces three-dimensional perturbations in the flow. As these perturbations convect to the separated region, they interact with the inflectional boundary layer, and trigger the Kelvin-Helmholtz instability that later leads to the development of roll-up vortices in the shear layer and to a breakdown of the laminar shear layer. The combined effect of wake forcing and surface roughness maintain the unsteadiness of the bubble. This unsteady behavior of the separated region differs from the individual effect of the wake study of [9]. In that study for the same wake passing period, the bubble finds time to regenerate itself. For the combined study presented here, the laminar separation bubble is unstable because of the accelerated flow that comes from the roughness openings. This accelerated flow disturbs the bubble and tries to maintain its unsteadiness. This effect becomes more apparent for the high wake passing frequency case (Figure 4.4b).

Figure 4.4 clearly shows that the disturbances which come from the wake are much stronger than the disturbances come from the roughness. So, to maintain the break up process of the separated region, disturbances which come from the roughness should be supported by disturbances come from the wake.

For the $\mathcal{R}3dWSt0.78$ case, the distance between the two wakes is too long, so perturbations that come from the roughness are not sufficient to maintain the unsteadiness of the bubble. However, for the $\mathcal{R}3dWSt1.55$ case, the distance between two wake is short enough to maintain the perturbation comes from the roughness. The laminar separation bubble never finds time to regenerate itself. Shortly, the combined effect which is treated in this problem behaves like a high frequency wake forcing case of [9].

The sequence of phase-averaged skin friction coefficient for cases $\mathcal{R}3dWSt0.78$ and $\mathcal{R}3dWSt1.55$ shown in Figures 4.5 and 4.6, respectively provide a clear view of what happens around the separated region. Phase averaging is performed by dividing each passing period, \mathcal{T} into ten equal subdivisions. Figures 4.5 and 4.6 present results for the phase intervals of $0\mathcal{T}, 0.1\mathcal{T}, 0.4\mathcal{T}$ and $0.6\mathcal{T}$.

Figures 4.5 and 4.6 illustrate the footprint of the vortices (red circles) on the wall. The existence of distinct peaks and troughs within the separated region is recognized, and these coincide with large-scale positive and negative perturbations of the streamwise velocity in the near-wall associated with the vortices. It is clear from these figures that, for the instance of $0\mathcal{T}$ when there is no wake in the domain, three roll-up vortices are seen. The incoming wake suppresses the regeneration of the laminar separation bubble and break up occurs. After the wake passes, roll-up vortices get bigger and stronger.

The phase-averaged flow properties of the individual wake forcing case ($\mathcal{W}St1.55$) for Strouhal number $St = 1.55$ is investigated by [9]. It is observed that the magnitude of the skin friction coefficient of the case $\mathcal{W}St1.55$ is higher compare to our case $\mathcal{R}3dWSt1.55$ where both roughness and wakes are considered. This could be explained through the fact that wakes break the roll-up vortices into small pieces, this makes an increase in the length of the LSB. Therefore, the wet area increases and the skin friction coefficient also increases. We can deduce, from the Figure 5 of [9] and Figure 4.6, that the surface roughness reduces the skin friction coefficient and the turbulent activity in the boundary layer.

Figures 4.7 and 4.8 illustrate the time-series evolution of the "transitional" structures. The roughness effect is clearly seen from the shape of the structures for all the time instances. These sinusoidal shape structures, induced due to the roughness, interact nonlinearly with the large amplitude KH vortices of the separated shear layer. The most striking feature is the very ordered structure of the flow after the wake passing for both cases, $\mathcal{R}3dWSt0.78$ and $\mathcal{R}3dWSt1.55$. The breakdown of the instantaneous high-shear layer vortices into smaller vortices is also observed for both cases.

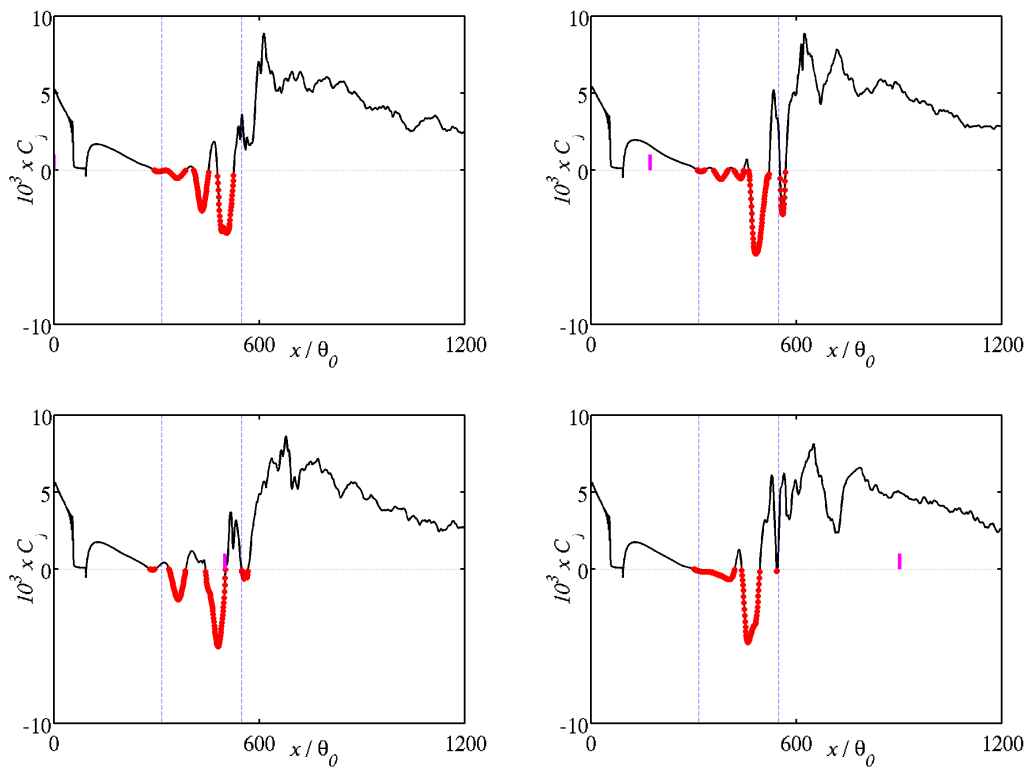


Figure 4.5: The phase-averaged skin friction coefficient over one forcing period for case $R3dWSt0.78$. The vertical thick solid line marks the location of the wake center.

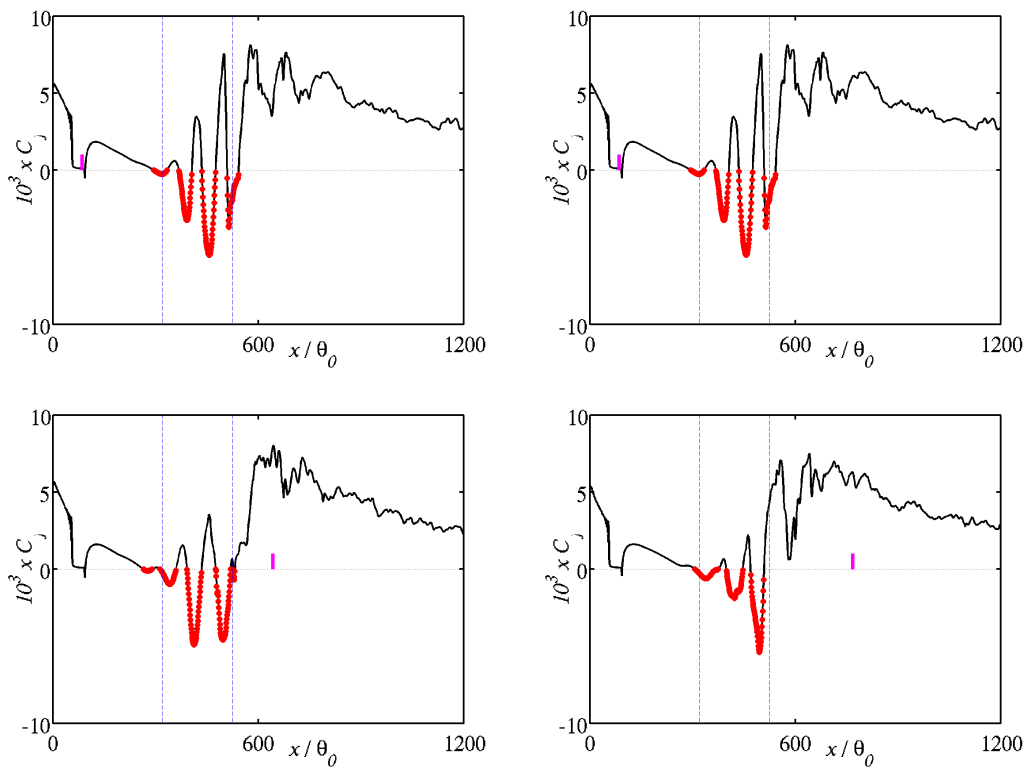


Figure 4.6: The phase-averaged skin friction coefficient over one forcing period for case $R3dWS1.55$. The vertical thick solid line marks the location of the wake center.

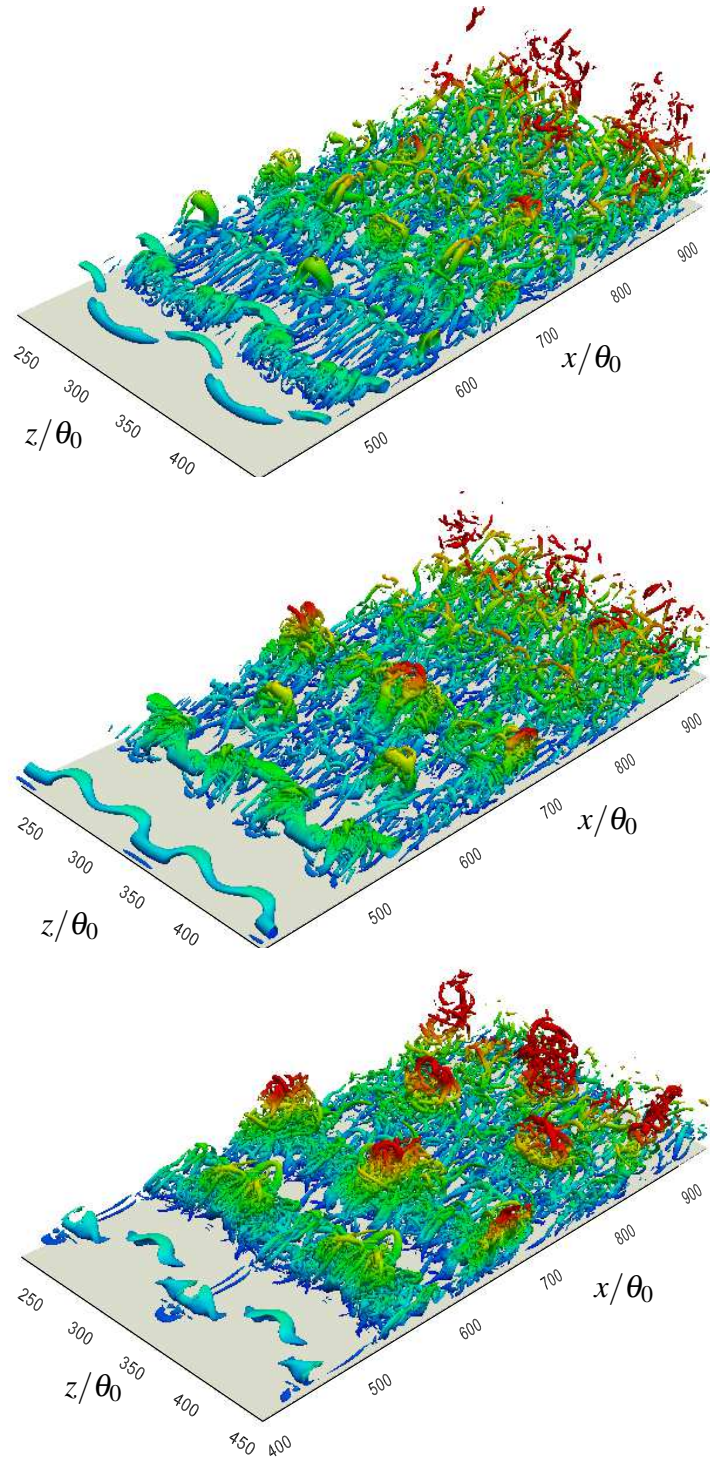


Figure 4.7: Evolution of the transitional structures of the $\mathcal{R}3dWSi0.78$ case at three different time instances $0\mathcal{T}$, $0.4\mathcal{T}$, $0.6\mathcal{T}$. The isosurface of the second-invariant of the velocity gradient tensor colored by the distance to the wall, from $y/\theta_0 = 0$ for the deepest blue, to $y/\theta_0 = 50$ for the brightest red. Flow is from bottom left to top right.

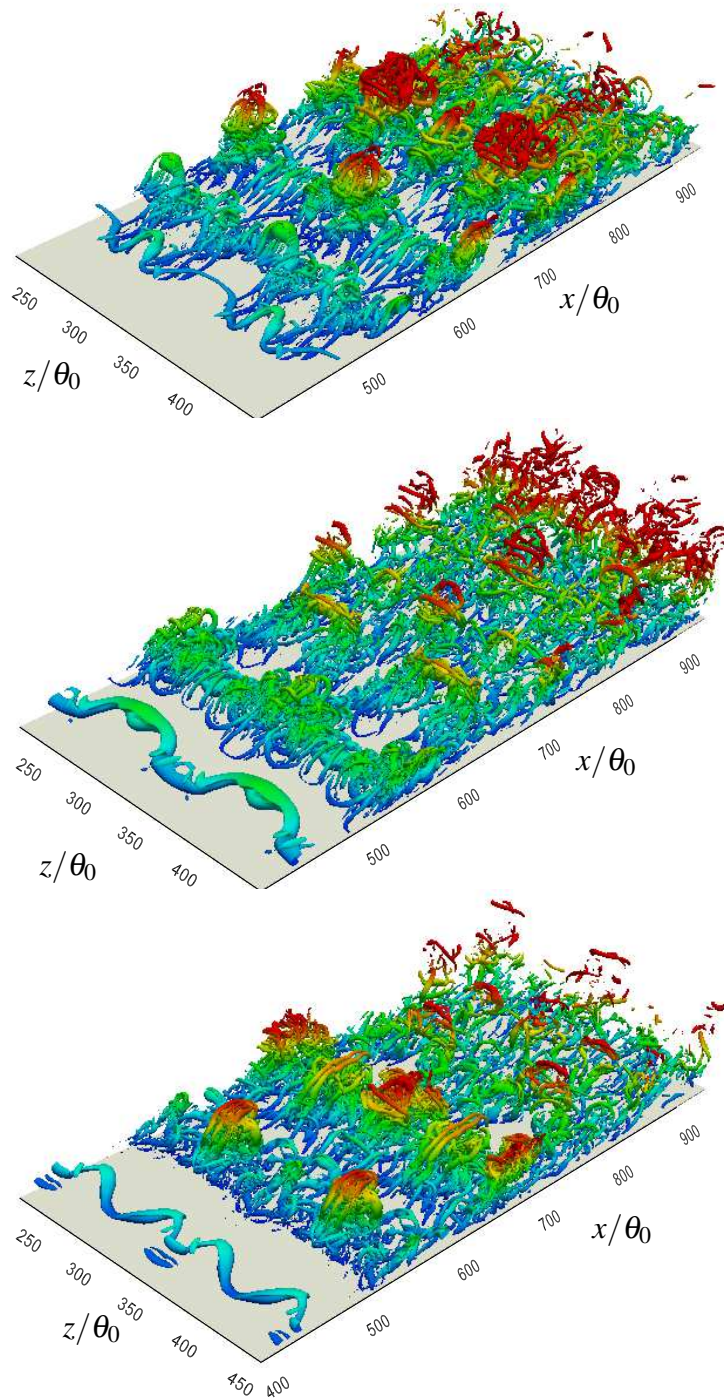


Figure 4.8: Evolution of the transitional structures of the $\mathcal{R}3dWSt1.55$ case at three different time instances $0\mathcal{T}$, $0.4\mathcal{T}$, $0.6\mathcal{T}$. The isosurface of the second-invariant of the velocity gradient tensor colored by the distance to the wall, from $y/\theta_0 = 0$ for the deepest blue, to $y/\theta_0 = 50$ for the brightest red. Flow is from bottom left to top right.

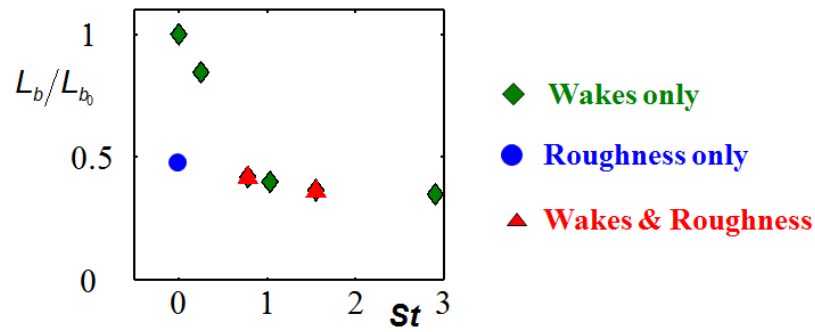


Figure 4.9: The effects of wake forcing (green diamond), surface roughness (blue circle), and combined effect of roughness and wake (red triangle) on the size of the separation bubble, L_b .

4.4 Summary

The combined effect of wake forcing and roughness on the control of separated boundary layers are studied in this chapter.

Figure 4.9 provides a summary of the cases presented in this chapter and in [8, 9]. Results indicate that the combined control parameters affect the development of the boundary layer, the transition mechanism and the size of the laminar separation bubble. The bubble size is found to be reduced almost 60% compared to the base case, and therefore the separation induced losses decreased significantly. Separation point moves downstream, early transition and reattachment is observed.

The unsteady forcing data indicates that if the forcing period is much lower than the time required for the bubble to recover itself after the wake passing, then the size of the bubble decreases significantly. Moreover, it is found that the roughness induces three-dimensional perturbations that slows down the regeneration of the separation bubble after the wake passing. However, for mean flow properties, the roughness effect is found to be negligible compared to the individual wake effect.

5. CONCLUSIONS AND FUTURE WORK

The wake forcing and surface roughness, as passive boundary layer control mechanisms, are examined numerically using direct numerical simulation approach. The laminar separation bubble of interest is formed on a flat plate boundary layer due to a strong adverse pressure gradient. The flow Reynolds number and streamwise pressure distribution are representative of the suction side of a T106C ultra-high-lift LPT blade.

The effect of roughness length with varying roughness height in the spanwise direction on the control of a separated boundary layer is investigated in chapter 3. Roughness elements are imposed to the problem as a sinusoidal function in the spanwise direction. Results have provided insight into the underlying mechanism for roughness-induced transition.

The spanwise-varying surface roughness pattern causes a two-fold change in the boundary layer; it increases the local disturbance level and it also causes local changes in the mean flow profile. The flow accelerates while passing through the openings of the roughness. This acceleration causes an increase in momentum transfer and delays the separation. Furthermore, the sinusoidal roughness pattern generates additional disturbances in the boundary layer that changes the growth of the disturbances in the separated shear layer. Roughness moves the reattachment point upstream, owing to early transition and hence increased wall-normal mixing. While the initial disturbance amplitudes are different for two roughness lengths, the long roughness induced disturbances are not enough to cause a significant difference in the mean flow. Results indicate that the mean flow characteristics are very similar for the two roughness lengths.

The combined effects of discrete surface roughness and unsteady wake forcing on the development of laminar separated boundary layer is studied in chapter 4. The numerical wakes designed to mimic the mean wake deficit created by a linear row

of cylinders moving in a direction perpendicular to the plate are superimposed at the inflow velocity profiles.

Results indicate that the laminar separation and turbulent transition are mainly affected by the combined effect of large-scale wake forcing and discrete roughness. The comparison between the individual influence of wakes and roughness on the separation indicates that the transition of the separated boundary layer with wakes occur almost at the same streamwise location as that induced by the roughness element. This indicates that the unsteady transition process and the growth rate of the disturbances are independent of the control mechanism. Similarly the unsteady forcing data indicates that if the forcing period is much lower than the time required for the bubble to recover itself after the wake passing, then the size of the bubble decreases significantly. The effect of the boundary layer trip, however, is found to be negligible compared to the wake effect. As a result, the mean flow statistics show almost similar trends for the unsteady smooth and rough cases. In conclusion, the separation bubble can be controlled by positioning the roughness element away from the separation bubble and introducing a large scale wake forcing.

We observe in this thesis that, surface roughness and wake forcing changes the transition dynamics of the separated boundary layer. Further investigation on the effect of these control mechanisms is needed to shed light on how they promote transition in the boundary layer. Also, examining momentum budgets and dissipation parameters are essential to understand the effects of wake forcing and surface roughness inside the boundary layer. Further research is also needed to understand the effect of distributed surface roughness shapes on the separated boundary layer.

REFERENCES

- [1] **Zhang, X.F. and Hodson, H.**, 2005. Combined effects of surface trips and unsteady wakes on the boundary layer development of and ultra-high-lift turbine blade, *ASME Journal of Turbomachinery*, **127**, 479–488.
- [2] **Hodson, H.P. and Howell, R.J.**, 2005. Bladerow interactions, transition and high-lift aerofoils in low-pressure turbine, *Annual Review of Fluid Mechanics*, **37**, 71–98.
- [3] **Montomoli, F., Hodson, H. and Haselbach, F.**, 2010. Effect of roughness and unsteadiness on the performance of a new low pressure turbine blade at low Reynolds numbers, *ASME Journal of Turbomachinery*, **132**, 1–9.
- [4] **Gaster, M.**, 1966. The structure and behaviour of laminar separation bubbles, *AGARD CP-4*, 813–854.
- [5] **Owen, P.R. and Klanfer, L.**, 1955. On the laminar boundary layer separation from the leading edge of a thin airfoil, *Royal Aircraft Establishment, UK, (C.P. No. 220)*.
- [6] **Lord, W.K., MacMartin, D.D. and Tillman, G.**, 2000. Flow control opportunities in gas turbine engines.
- [7] **Gad-El-Hak, M.**, 2000. *Flow Control; Passive, Active and Reactive Flow Management*, Cambridge University Press.
- [8] **Simens, M.P. and Gungor, A.G.**, 2014. Effect of surface roughness on laminar separated boundary layers, *Journal of Turbomachinery*, **136**, 1–8.
- [9] **Gungor, A.G., Simens, M.P. and Jiménez, J.**, 2012. Direct numerical simulations of wake-perturbed separated boundary layers, *ASME Journal of Turbomachinery*, **134**, 1–9.
- [10] **Roberts, S. and Yaras, M.**, 2005. Boundary layer transition affected by surface roughness and freestream turbulence, *Journal of Fluids Engineering*, **127**, 449–457.
- [11] **Malkiel, E. and Mayle, R.**, 1996. Transition in a separation bubble, *Journal of Turbomachinery*, **118**, 752–759.
- [12] **Volino, R.J.**, 2012. Effect of unsteady wakes on boundary layer separation on a very high lift low pressure turbine airfoil, *ASME Journal of Turbomachinery*, **134(1)(011011)**.

- [13] **Marxen, O. and Rist, U.**, 2004. The effect of spanwise-modulated disturbances on transition in a 2D separated boundary layer, *AIAA Journal*, **42** (8), 937–944.
- [14] **Theofilis, V., Hein, S. and Dallmann, U.**, 2000. On the origins of three-dimensionality and unsteadiness in the laminar separation bubble, *Philosophical Transactions of the Royal Society (London) Series A*, **358**, 3229–3246.
- [15] **Wörner, A., Rist, U. and Wagner, S.**, 2002. Influence of humps and steps on the stability characteristics of a 2D laminar boundary layer, *AIAA-Paper 2002-0139*.
- [16] **Lorenz, M., Schulz, A. and Bauer, J.H.**, 2012. Experimental study of surface roughness effects on a turbine airfoil in a linear cascade-Part II: Aerodynamic losses, *ASME Journal of Turbomachinery*, **134**, 1–11.
- [17] **Kaneda, Y., Ishihara, T., Yokokawa, M. and Uno, A.**, 2003. Energy dissipation rate and energy spectrum in high resolution direct numerical simulation of turbulence in a periodic box., *Physics of Fluids*, **15**, L21–L24.
- [18] **Jimenez, J.**, 2003. Computing high-reynolds-number turbulence: will simulations ever replace experiments?, *Journal of Turbulence*, **4**(22).
- [19] **Hoyas, S. and Jimenez, J.**, 2006. Scaling of the velocity fluctuations in turbulent channels up to $Re_\tau = 2003$, *Physics of Fluids*, **18**(011702).
- [20] **Sillero, J.A., Jiménez, J. and Moser, R.D.**, 2013. One-point statistics for turbulent wall-bounded flows at Reynolds numbers up to $\delta^+ \approx 2000$, *Physics of Fluids*, **423**, 183–226.
- [21] **Moin, P. and Mahesh, K.**, 1998. Direct numerical simulation: A tool in turbulence research, *Annual Review of Fluid Mechanics*, **30**, 539–578.
- [22] **Pope, S.B.**, 2000. *Turbulent Flows*, Cambridge University Press.
- [23] **Simens, M.P., Jiménez, J., Hoyas, S. and Mizuno, Y.**, 2009. A high-resolution code for turbulent boundary layers, *Journal of Computational Physics*, **228**, 4218–4231.
- [24] **Harlow, F.H. and Welch, J.E.**, 2005. Numerical calculation of time-dependent viscous incompressible flow of fluid with free surface, *Physics of Fluids*, **8**, 2182–2189.
- [25] **Perot, J.**, 1993. An analysis of the fractional step method, *Journal of Computational Physics*, **108**, 51–58.
- [26] **Lele, S.**, 1992. Compact Finite Difference Schemes with Spectral-like Resolution, *Journal of Computational Physics*, **103**, 16–42.

- [27] **Fadlun, E.A., Verzicco, R., Orlandi, P. and Mohd-Yusof, J.**, 2000. Combined immersed-boundary finite-difference methods for three-dimensional complex flow simulations, *Journal of Computational Physics*, **161**, 35–60.
- [28] **Uhlmann, M.**, 2005. An immersed boundary method with direct forcing for the simulation of particulate flow, *Journal of Computational Physics*, **209**, 448–476.
- [29] **Bandringa, H.**, 2010. Immersed Boundary Methods, *Master Thesis in Applied Mathematics, University of Groningen, Netherlands*.
- [30] **Schlichting, H. and Gersten, K.**, 2000. Boundary Layer Theory, McGraw Hill.
- [31] **Thwaites, B.**, 1949. Approximate calculation of the laminar boundary layer, *Royal Aeronautical Society*, **1**, 61–85.
- [32] **Hunt, J.C.R., Wray, A.A. and Moin, P.**, 1988. Eddies, stream, and convergence zones in turbulent flows, *Center for Turbulence Research Report*, 193–208.
- [33] **Spalart, P. and Strelets, M.**, 2000. Mechanism of transition and heat transfer in a separation bubble, *Journal of Fluid Mechanics*, **403**, 329–349.
- [34] **Brinkerhoff, J. and Yaras, M.**, 2011. Interaction of viscous and inviscid instability modes in separation-bubble transition, *Physics of Fluids*, **23(12)(124102)**.
- [35] **Watmuff, J.**, 1999. Evolution of a wave packet into vortex loops in a laminar separation bubble, *Journal of Fluid Mechanics*, **397**, 119–169.
- [36] **Brandt, L. and Lange, H.C.**, 2008. Streak interactions and breakdown in boundary layer flows, *Physics of Fluids*, **20(2)(024107)**.
- [37] **Kloker, M. and Bestek, H.**, 1992. Direct spatial simulation of laminar-turbulent transition in a boundary layer with strong adverse pressure gradient, *Proc. DGLR-Jahrestagung*, **III**, 1517–1526.
- [38] **Rogers, M. and Moin, P.**, 1992. The three-dimensional evolution of a plane mixing layer: the Kelvin-Helmholtz rollup, *Journal of Fluid Mechanics*, **243**, 183–226.
- [39] **Simens, M.P.**, 2009. The study and control of wall bounded flows, *Ph.D. Thesis, Universidad Politécnica de Madrid, Spain*.
- [40] **Karaca, S., Simens, M.P. and Gungor, A.G.**, 2013. Direct numerical simulation of combined effects of wake and discrete surface roughness on separated boundary layers, 7th Ankara International Aerospace Conference, METU, Ankara, Turkey.
- [41] **Alam, M. and Sandham, N.**, 2000. Direct numerical simulation of ‘short’ laminar separation bubbles with turbulent reattachment, *Journal of Fluid Mechanics*, **410**, 1–28.

- [42] **Diwan, S. and Ramesh, O.**, 2009. On the origin of the inflectional instability of a laminar separation bubble, *Journal of Fluid Mechanics*, **629**, 263–298.
- [43] **Curle, N. and Skan, S.W.**, 1957. Approximate methods for predicting separation properties of laminar boundary layers, *Aero. Q.*, **8**, 257–268.

CURRICULUM VITAE

Name Surname: Süleyman Karaca

Place and Date of Birth: Karamürsel / 1988

Address: Faculty of Aeronautics and Astronautics, Istanbul Technical University, 34469 Istanbul, Turkey

E-Mail: karacasu@itu.edu.tr

B.Sc.: ITU, Aeronautical Engineering, 2011

M.Sc.: ITU, Aeronautics and Astronautics Engineering, 2014

List of Publications and Patents:

- Kayhan, A., Karaca, S., and Şahin, M., "An Integral Equation Approach for the Solution of the Stokes Flow with Hermite Surface", 18th Ulusal Mekanik Kongresi, Manisa, Türkiye, 2013.
- Süleyman Karaca, "An Integral Equation for the Solution of Three-Dimensional Stokes Flows", Istanbul Technical University, Aeronautical Engineering, Bachelor Thesis, 2011.

PUBLICATIONS/PRESENTATIONS ON THE THESIS

- Gungor, A.G., Karaca, S., and Simens, M.P., "The influence of roughness length on the control of separation bubbles," 10th International ERCOFTAC Symposium on Engineering Turbulence Modeling and Measurements, Malaga, Spain, 2014.
- Gungor, A.G., Simens, M.P., and Karaca, S., "Direct numerical simulation of roughness and unsteady wake effect on separated boundary layers", 14th European Turbulence Conference, Lyon, France, 2013.
- Karaca, S., Simens, M.P., and Gungor, A.G., "Direct numerical simulation of combined effects of wake and discrete surface roughness on separated boundary layers," 7th Ankara International Aerospace Conference, Ankara, Turkey, 2013.
- Karaca, S., and Gungor A.G., "Gaz türbini pallerindeki akış ayrılmasına iz ve pürüzlülük etkilerinin DNS yöntemiyle incelenmesi ", 18th Ulusal Mekanik Kongresi, Manisa, Türkiye, 2013.